NASA/TM—2019-217822/PART4

Buckling Testing and Analysis of Honeycomb Sandwich Panel Arc Segments of a Full-Scale Fairing Barrel
Part 4: Six-Ply Out-of-Autoclave Facesheets

David E. Myers and Evan J. Pineda
Glenn Research Center, Cleveland, Ohio

Sotirios Kellas and Genevieve D. Dixon
Langley Research Center, Hampton, Virginia

Daniel N. Kosareo
Vantage Partners, LLC, Brook Park, Ohio

December 2019

NASA STI Program . . . in Profile

Since its founding, NASA has been dedicated to the advancement of aeronautics and space science. The NASA Scientific and Technical Information (STI) Program plays a key part in helping NASA maintain this important role.

The NASA STI Program operates under the auspices of the Agency Chief Information Officer. It collects, organizes, provides for archiving, and disseminates NASA's STI. The NASA STI Program provides access to the NASA Technical Report Server—Registered (NTRS Reg) and NASA Technical Report Server—Public (NTRS) thus providing one of the largest collections of aeronautical and space science STI in the world. Results are published in both non-NASA channels and by NASA in the NASA STI Report Series, which includes the following report types:

- TECHNICAL PUBLICATION. Reports of completed research or a major significant phase of research that present the results of NASA programs and include extensive data or theoretical analysis. Includes compilations of significant scientific and technical data and information deemed to be of continuing reference value. NASA counter-part of peer-reviewed formal professional papers, but has less stringent limitations on manuscript length and extent of graphic presentations.

- TECHNICAL MEMORANDUM. Scientific and technical findings that are preliminary or of specialized interest, e.g., "quick-release" reports, working papers, and bibliographies that contain minimal annotation. Does not contain extensive analysis.

- CONTRACTOR REPORT. Scientific and technical findings by NASA-sponsored contractors and grantees.

- CONFERENCE PUBLICATION. Collected papers from scientific and technical conferences, symposia, seminars, or other meetings sponsored or co-sponsored by NASA.

- SPECIAL PUBLICATION. Scientific, technical, or historical information from NASA programs, projects, and missions, often concerned with subjects having substantial public interest.

- TECHNICAL TRANSLATION. English-language translations of foreign scientific and technical material pertinent to NASA's mission.

For more information about the NASA STI program, see the following:

- Access the NASA STI program home page at http://www.sti.nasa.gov

- E-mail your question to help@sti.nasa.gov

- Fax your question to the NASA STI Information Desk at 757-864-6500

- Telephone the NASA STI Information Desk at 757-864-9658

- Write to:
  NASA STI Program
  Mail Stop 148
  NASA Langley Research Center
  Hampton, VA 23681-2199

Buckling Testing and Analysis of Honeycomb Sandwich Panel Arc Segments of a Full-Scale Fairing Barrel
Part 4: Six-Ply Out-of-Autoclave Facesheets

David E. Myers and Evan J. Pineda
Glenn Research Center, Cleveland, Ohio

Sotirios Kellas and Genevieve D. Dixon
Langley Research Center, Hampton, Virginia

Daniel N. Kosareo
Vantage Partners, LLC, Brook Park, Ohio

Acknowledgments

Level of Review: This material has been technically reviewed by technical management.

Buckling Testing and Analysis of Honeycomb Sandwich Panel Arc Segments of a Full-Scale Fairing Barrel
Part 4: Six-Ply Out-of-Autoclave Facesheets

David E. Myers and Evan J. Pineda
National Aeronautics and Space Administration
Glenn Research Center
Cleveland, Ohio 44135

Sotirios Kellas and Genevieve D. Dixon
National Aeronautics and Space Administration
Langley Research Center
Hampton, Virginia 23681

Daniel N. Kosareo
Vantage Partners, LLC
Brook Park, Ohio 44142

Summary

Four honeycomb sandwich panel types, representing 1/16th arc segments of a 10-m-diameter barrel section of the heavy-lift launch vehicle (HLLV), were manufactured and tested under the NASA Composites for Exploration (CoEx) program and the NASA Constellation Ares V program. Two configurations were chosen for the panels: six-ply facesheets with 1.125-in. honeycomb core and eight-ply facesheets with a 1-in. honeycomb core. Additionally, two separate carbon fiber/epoxy material systems were chosen for the facesheets: in-autoclave (IA) CYCOM® IM7/977-3 (Cytec) and out-of-autoclave (OOA) CYCOM® T40-800B/5320-1 (Cytec). Smaller 3- by 5-ft panels were cut from the 1/16th barrel sections. These panels were tested under compressive loading at the NASA Langley Research Center. Furthermore, linear eigenvalue and geometrically nonlinear finite element analyses (FEAs) were performed to predict the compressive response of each 3- by 5-ft panel. This manuscript summarizes the experimental and analytical modeling efforts pertaining to the panels composed of six-ply, T40-800B/5320-1 facesheets (referred to as Panel D). To improve the robustness of the geometrically nonlinear finite element model, measured surface imperfections were included in the geometry of the model. Both the linear and nonlinear models yield good qualitative and quantitative predictions. Additionally, it was correctly predicted that the panel would fail in buckling prior to failing in strength. Furthermore, three-dimensional effects on the compressive response of the panel were studied.

1.0   Introduction

Two manufacturing demonstration honeycomb sandwich panels (1/16th arc segments of the 10-m-diameter cylinder) were fabricated under the NASA Composites for Exploration (CoEx) program and two under the NASA Constellation Ares V program. All four panels were manufactured by Hitco Carbon Composites. Two distinct configurations were chosen for the panels. The first configuration, fabricated under the CoEx program, was composed of eight-ply facesheets with a $[45°/90°/–45°/0°]_s$ layup and 1-in. aluminum honeycomb core. The second configuration, fabricated under the Constellation Ares V

program, consisted of six-ply facesheets with a [60°/–60°/0°]$_s$ stacking sequence and a 1.125-in. aluminum honeycomb core. In addition to the two configurations, two different carbon fiber/epoxy facesheet material systems were chosen for the panels: in-autoclave (IA) IM7/977-3 and out-of-autoclave (OOA) T40-800B/5320-1. It should also be noted that the honeycomb used in the eight-ply panels was machined to match the curvature of the panel, while the honeycomb used in the six-ply panels was flat. Additionally, in each panel, an adhesive splice joint was used to join discontinuous sections of the honeycomb core.

Following delivery to Langley, nondestructive evaluation (NDE) inspection (including ultrasonic testing and flash thermography) was performed on the full manufacturing demonstration panel. The results of the NDE guided the decision on where to cut 36-in.-wide by 62-in.-long sections for edgewise compression buckling tests. Following removal of the 36- by 62-in. panels from the manufacturing demo, the panels were reinspected using infrared (IR) thermography to ensure that no damage had occurred. In preparation for testing, the load introduction ends of the panels were potted in 1-in.-thick aluminum end plates. The purpose of the end plates was to stabilize the facesheets and prevent local crushing, thus generating a predictable and repeatable end condition. As such, the panels are referred to as 3 by 5 ft, according to the acreage dimensions of the test panels. Preliminary finite element analysis (FEA) indicated that no additional reinforcement was needed at the load introduction ends of the panels. A summary of the five 3- by 5-ft panels that were tested is given in Table I.

The current document provides details specifically pertaining to Panel D, which consisted of six-ply facesheets composed of OOA T40-800B/5320-1 and a 1.125-in. honeycomb core. Similarly, separate documents have been prepared for Panels A, B, and C. The remaining subsections of Section 1.0 summarize the experimental and modeling objectives pertaining to all four panels. Section 2.0 provides details on Panel D. In Section 3.0, several approaches that were used to predict the buckling load of Panel D are described. The experimental and numerical results are presented in Section 4.0. Finally, results from a three-dimensional model are given in Section 5.0. Previous studies (Myers et al., 2013 and Pineda et al., 2013) performed some sensitivity analysis on similar panel configurations. It is assumed that the results from these studies are also applicable to this panel.

1.1   Test Objectives

The primary objective of the test is to measure the maximum compressive load carrying capability (buckling load) of each 3- by 5-ft panel and to provide data for analysis correlation and validation. A secondary objective is to study the effect of manufacturing defects on the deformation and buckling load.

TABLE I.—DETAILS OF FOUR 5-ft-TALL BY 3-ft-WIDE PANELS CUT FROM 1/16th ARC
SEGMENTSOF 10-m BARREL SECTION THAT WERE LOADED UNTIL BUCKLING

3- by 5-ft panel I.D.	1/16th arc-segment panel I.D.	Facesheet material	Facesheet layup	Core thickness, in.
Panel A	8000-CMDP	IM7/977-3 (IA[a])	[45°/90°/–45°/0°]$_s$	1.000 (curved)
Panel B-1	MTP-6003	IM7/977-3 (IA)	[60°/–60°/0°]$_s$	1.125 (flat)
Panel B-2	MTP-6000	IM7/977-3 (IA)	[60°/–60°/0°]$_s$	1.125 (flat)
Panel C	8010-CMDP	T40-800B/5320-1 (OOA[b])	[45°/90°/–45°/0°]$_s$	1.000 (curved)
Panel D[c]	MTP-6010	T40-800B/5320-1 (OOA)	[60°/–60°/0°]$_s$	1.125 (flat)

[a]In-autoclave.
[b]Out-of-autoclave.
[c]Panel being studied in this report.

1.2   Test Success Criteria

The test will be considered successful if each of the following criteria are met:

(1) All critical instrumentation is fully operational during the test.
(2) The loads are applied as described in this document.
(3) The maximum attained load and all associated data are recorded and saved in the desired format.

1.3   Modeling Objectives

The primary modeling objective is to predict the buckling load and structural response of each 3- by 5-ft panel as accurately as possible using standard, commercially available analysis tools. A linear eigenvalue baseline, obtained from the finite element method (FEM), will be compared to the experiment. More sophisticated, progressive collapse analyses, incorporating nonlinear geometric effects and the measured geometric imperfections of the panel surfaces, will be executed in an attempt to improve the baseline numerical (FEM) prediction. Additionally, linear strength analyses will be performed to ensure that predicted buckling occurs before expected strength failure. Finally, parametric studies will be performed to determine the sensitivity of the buckling load of the panel to varying degrees of imperfections, including as manufactured geometry, fiber angle misalignment, and loading eccentricity.

1.4   Modeling Success Criteria

The modeling will be considered successful if each of the following criteria are met:

(1) The buckling load is predicted within 20 percent.
(2) The buckling mode and direction is predicted accurately.
(3) Local strain fields correlate well qualitatively with visual imaging data measured during the experiment.

2.0   1/16th Panel Description

The 1/16th fabrication demo panel was constructed on a concave composite tool (5 m radius of curvature) using an automated tape laying process. The preimpregnated (prepreg) tape was composed of unidirectional fibers and was 6 in. wide. The prepreg contained T40-800B fibers and CYCOM® 5320 epoxy (Cytec). The stacking sequence of the facesheets was $[60°/–60°/0°]_s$. The facesheets were bonded to the 1.125-in.-thick aluminum core using FM® 300 film adhesive (Cytec), 0.08 lb/ft². The aluminum honeycomb core was flat, not machined, to match the curvature of the tool. The facesheets and core adhesive were co-cured in a single autoclave cycle. The aluminum core was HexWeb® 5052 (Hexcel®), 0.0007 in. thick with a 0.125-in. cell size, and a density of 3.1 pcf. An adhesive splice was needed to join discontinuous sections of the core because the 1/16th barrel section panel dimensions exceeded the size of the premanufactured core. A Hysol® EA 9396.6MD foaming adhesive (Henkel Corporation) was used to fill the gap between the two pieces of aluminum core. Previous analyses incorporating the adhesive core splice determined that the addition of the splice would not introduce local failure in the facesheets prior to buckling in the panels. A photograph of the manufacturing demonstration 1/16th arc segment (of a 5-m outside radius cylinder) panel is shown in Figure 1.

Figure 1.—Cured 1/16th arc segment panel and tool it was molded on.

2.1 Test Specimen Description

One 35.55-in.-wide (chord) by 62.0-in.-long test specimen was machined from the manufacturing demo panel following NDE. The end plates were 1-in.-thick aluminum plates and had a slot in the shape of the specimen's cross section machined in the center. The slot width and length were such that, when centered, the specimen had a clearance of 0.5 in. around the perimeter. After the specimen end was centered in the slot and squared, it was potted with UNISORB® V-100 epoxy grout. When both ends were potted and following the cure, the specimen ends were machined flat and parallel to within ±0.0025 in. A photograph of the test specimen with potted ends is shown in Figure 2. The potted dimensions of the T40-800B/5320-1 panel are shown in Figure 3. In addition to the overall dimensions, Figure 3 shows the relative position of the core splice with respect to the panel ends. For complete details on the CoEx experimental efforts, see Kellas, et al. (2012).

Once potted, strain gages were affixed to the inner diameter (I.D.) and outer diameter (O.D.) surfaces of the panel, as shown in Figure 4. The even-numbered gages were located on the I.D. while the odd-numbered gages were located on the O.D. These gages were monitored and the strains were recorded during loading of the panel. The panel was tested at Langley in a servo-hydraulic test frame. The panel was secured between two loading platens, with the bottom platen being fixed and the top platen allowed to move in the y-direction. The panel was loaded in compression until catastrophic failure occurred. Additional instrumentation included three direct-current displacement transducers (DCDTs) used to measure the global, axial deformation of the panel, and a load cell attached to the load platen to measure the applied load. Finally, the panels were painted using a speckle pattern for photogrammetric measurements. Visual image correlation (VIC) was employed to obtain full-field strain measurements during the test as well as high-speed video.
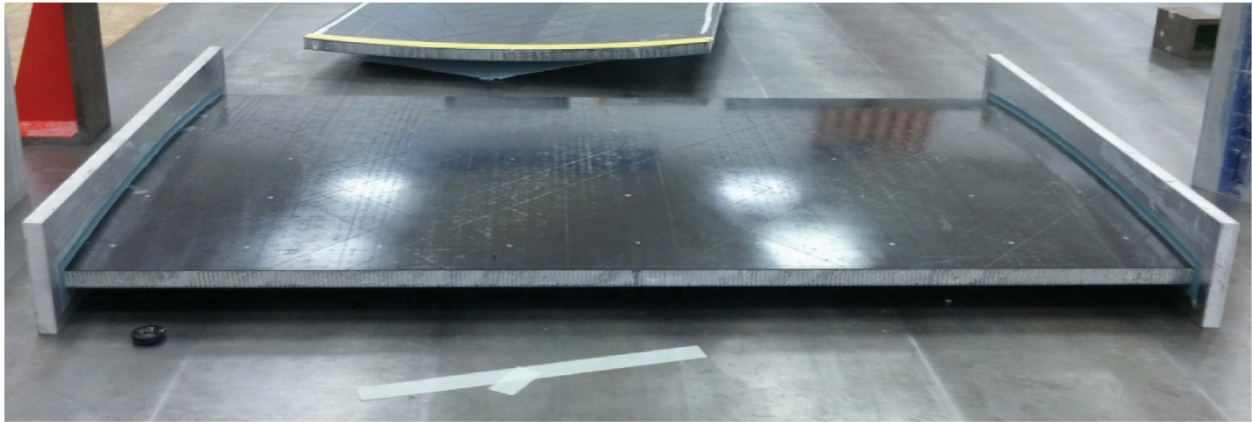
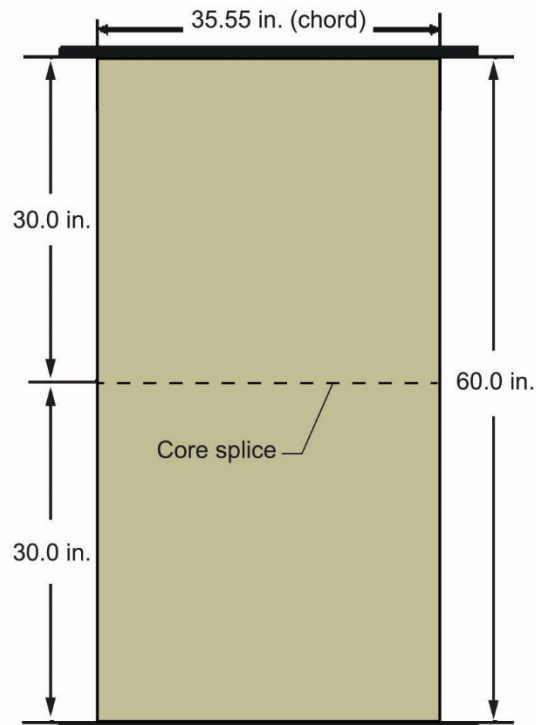Figure 2.—Test panel with potted aluminum end plates.

Figure 3.—Potted specimen dimensions. Note that
outside surfaces of aluminum end plates were
machined flat and parallel. Position of core
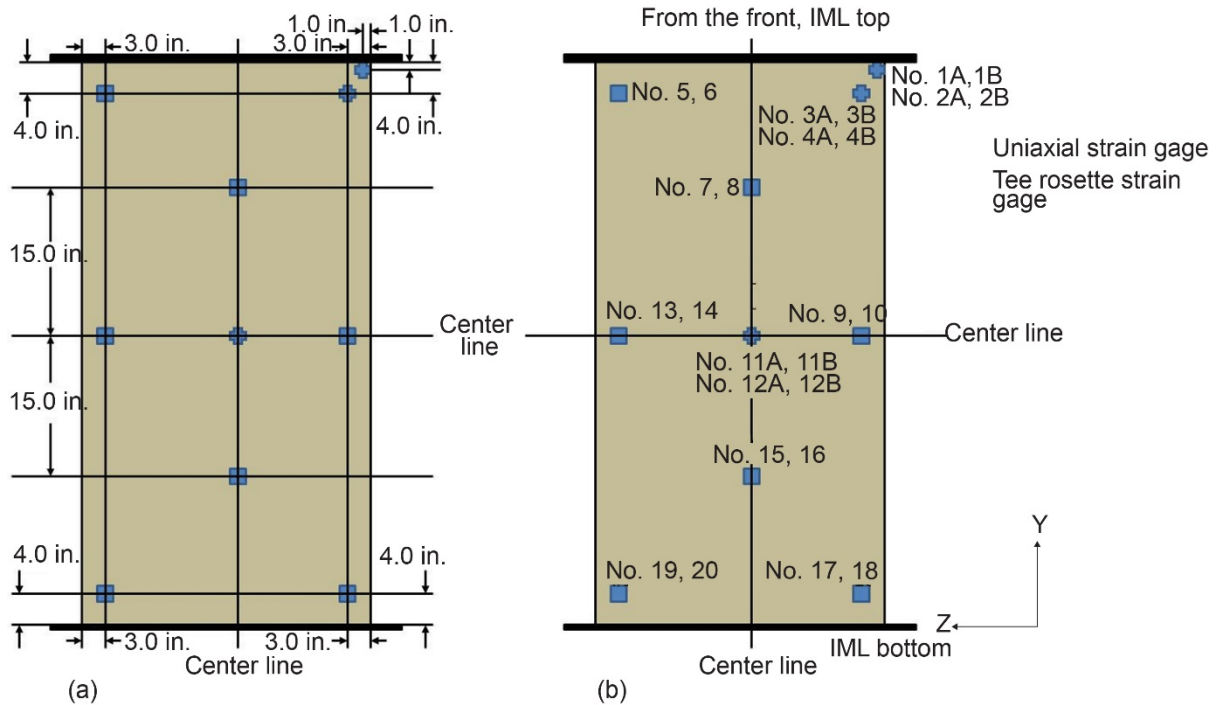splice is also shown relative to inside surface of
aluminum end plates.

Figure 4.—Panel configuration. (a) Panel geometry. (b) Strain gage location and nomenclature. All gages are back-to-back pairs and referenced numbers 1, 2; numbers 3, 4; and so forth. Odd numbered gages are located along O.D. surface. Even numbered gages are located along I.D., or IML, surface. "A" designation corresponds to lateral and "B" designation to axial direction.

3.0   Finite Element Analysis (FEA) Description

Pretest predictions of the buckling load for Panel D were determined using the commercially available FEM software package Abaqus (Dassault Systèmes). Figure 5 shows the test panel geometry used in the FEM model. The panel was modeled as 60 in. tall (section between the aluminum end plates) and 36.22 in. along the arc (36.17 in. along the chord) using two-dimensional layered shell elements. The shells were offset so that the geometry of the model represented the O.D. surface of the panel. Note that the FEM panel dimensions were chosen to represent an assumed cord length for the I.D. of 36 in., whereas the actual cord length of the I.D. of the panel was 35.55 in. (see Figure 3). The 1-in. sections of the panel on the top and bottom that were supported in the potting material were not modeled. The element size was 1 by 1 in., and the model was comprised of 2,257 nodes and 2,160 reduced integration shell elements. All three displacements and all three rotations were fixed along the bottom edge of the panel. The same boundary condition was applied to the top edge, except that a displacement was applied in the negative y-direction.

The stacking sequence of the facesheets was $[60°/0°/–60°]_s$ with 0.0053-in. plies. The T40-800B/5320-1 elastic properties and allowables (used in strength analysis) were obtained from the Orion materials database and are not shown as they are International Traffic in Arms Regulations (ITAR) restricted (Lockheed Martin, 2010). The aluminum honeycomb properties were obtained from the database included with the commercially available structural sizing software, HyperSizer® (Collier Research Corporation), and are presented in Table II. The in-plane normal and shear stiffnesses were reduced from 75 ksi to $1×10^{-3}$ ksi since the in-plane load carrying capability of the honeycomb is typically neglected in honeycomb sandwich panel analysis.
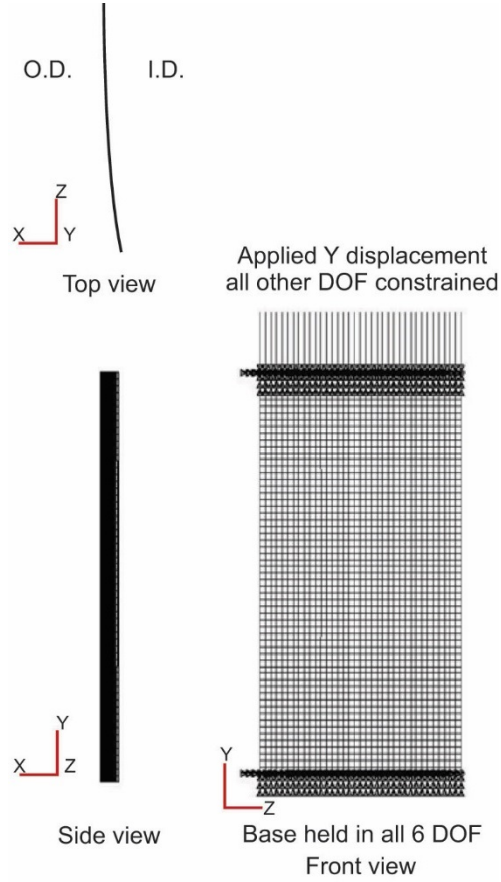
Figure 5.—Panel geometry with boundary conditions.

TABLE II.—Al HONEYCOMB MATERIAL
PROPERTIES, 3.1 pcf, 1/8 in.-5052-0.0007

Property	Value
E_1, ksi	1×10^{-3}
E_2, ksi	1×10^{-3}
ν_{12}	0.333
G_{12}, ksi	1×10^{-3}
G_{1Z}, ksi	45.0
G_{2z}, ksi	22.0
ρ, pcf	3.10
F_{t1}, ksi	0.200
F_{c1}, ksi	0.200
F_{t2}, ksi	0.200
F_{c2}, ksi	0.200
F_{s12}, ksi	0.090

To arrive at a baseline buckling failure prediction, a linear eigenvalue buckling analysis was performed in Abaqus. This preliminary analysis was executed for two reasons. First, the analysis provides a reasonable estimate of what the nonlinear analysis should predict as the panel buckling load with an efficient, quick turnaround. Second, this is the typical method of calculating buckling loads for flight structures, and it is informative to compare the results to the experimental buckling load and the buckling loads obtained from higher fidelity models.

In addition, to improve numerical predictions, it was also pertinent to predict which direction (toward the I.D. or O.D.) the panel would buckle as a DCDT was to be placed to measure the out-of-plane displacement of the panel and severe displacement in the unexpected direction would damage the gage. The eigenvectors obtained from an eigenvalue analysis are in an arbitrary direction and do not indicate the direction in which the panel would buckle. Therefore, a geometrically nonlinear static analysis was performed in Abaqus to arrive at a more accurate buckling load and determine the direction of buckling correctly.

Hause et al. (1998, 2000), Hilburger et al. (2001), Hilburger and Starnes, Jr. (2002), Lynch et al. (2004), and Schultz and Nemeth (2010) have shown that FEM simulations of progressive collapse incorporating geometric nonlinearities are extremely sensitive to the geometric imperfections in the panel. Thus, it was desired to use some measure of the actual imperfections of the panel and include them in the model. Preliminary photogrammetry data of the panel showed that the bag side (I.D.) surface contained some initial imperfections that were biased toward the I.D. On the O.D., or the tool side, the surface imperfections were sinusoidal in nature. Herein, these surface imperfections are referred to as the bow shape of the panel. In the progressive collapse analyses, the bow data from the bag side of the panel was used to incorporate geometric imperfections into the model. Figure 6 shows all the out-of-plane (radial) imperfection, or bow, data measured using VIC. The data are shown as a function of vertical position on the panel (height) at given intervals circumferentially along the I.D. arc.

The raw photogrammetry data was processed to arrive at a single curve, shown in Figure 7 (note that Figure 7 is rotated 90° clockwise, relative to Figure 6), and was used to create the FEM model geometry by sweeping it circumferentially along the arc of the panel. The data was first averaged, shown as the black line average in Figure 6. Then the data rotated such that both the top and bottom had an out-of-plane bow displacement of 0 in. Finally, the data was then scaled (60-in. total height of photogrammetry data) so that it covered the full 60 in. of the panel, as is displayed on Figure 6 as the stretched red line and in Figure 7. This data were used to approximate the bow shape in the model. The approximated bow geometry was then swept along an arc of radius 198 in. and 10.48°, providing a uniform tangential panel cross section. Realistically, the cross section of the panel varies in the circumferential direction, as shown in Figure 6, but it was assumed that the imperfect, but uniform, cross section used in the numerical model was sufficient to capture the primary effects of the geometric imperfections in the panel.

Finally, linear static solution in MacNeal-Schwendler Corporation NASA STRucture ANalysis (MSC Nastran) (SOL 101) was executed to determine the strength margins of safety at the time of onset of buckling. A similar analysis was performed in HyperSizer®. These results were used to determine whether the failure of the panel was stiffness critical (buckling) or strength critical (local facesheet or core failure).
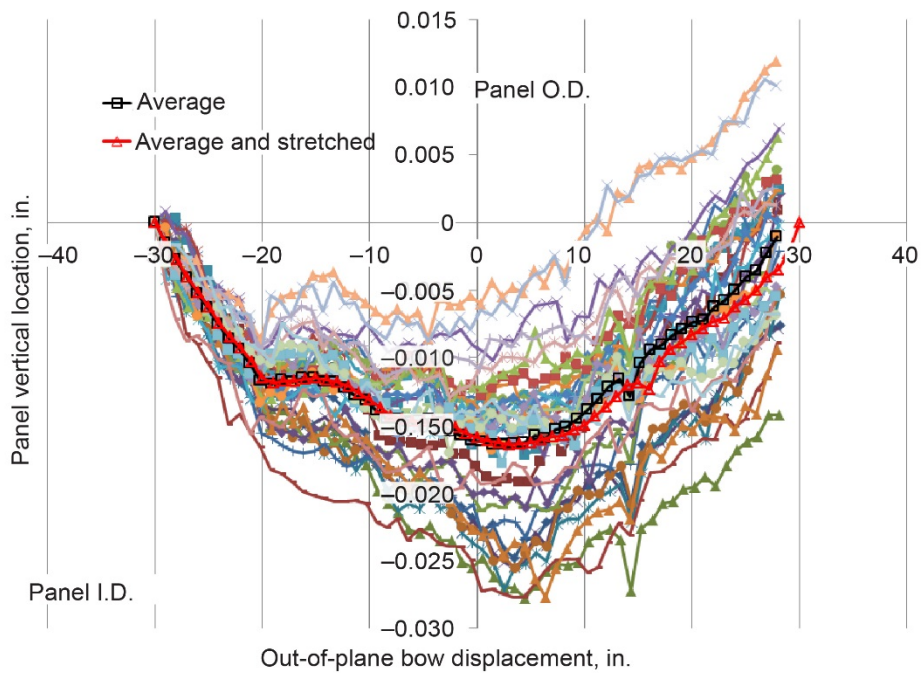
Figure 6.—Out-of-plane displacement data from visual image correlation as function of vertical position (height) taken circumferentially along panel arc.
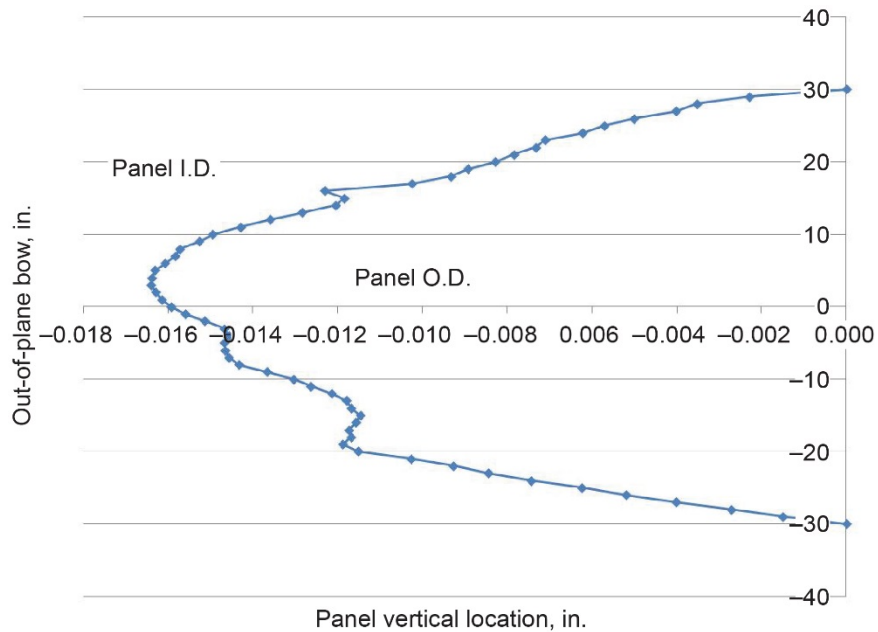

Figure 7.—Imperfection, or bow, data from bag side (O.D.) of panel. Data were taken vertically along height of panel in horizontal center of panel.

4.0   Test and Analysis Comparison

To determine the panel buckling load, a method from Singer, et al. (1998), shown in Figure 8, was used. This method utilizes global load versus local strain gage data (axial strain) to mark the onset of buckling. In Figure 8, a vertical tangent line intersects the load-strain curve at a local strain where the local strain increment reverses, which is designated as the local buckling strain. The load corresponding to that local strain is designated as the buckling load. It should be noted that the buckling strain, and hence buckling load, can only be determined at monitored locations and therefore, can actually be lower than the lowest measured value. Thus, the postulated buckling load is somewhat subjective and based upon the location where the strains are being monitored for reversal. Test data for gages 1 and 2 exhibited strain reversal at the lowest applied edge load. This load, 63,947 lb, will be considered the buckling load, and the numerical buckling loads will be determined from the global load versus local strain plots obtained from points on the models corresponding to these gage locations.

As mentioned previously, the full panel was inspected via NDE and the 3- by 5-ft specimen (Panel D) was cut from an area were no damage was noted. In addition, measurements were taken to ensure proper alignment of the panel prior to testing. However, the test specimen failed catastrophically, as shown in Figure 9 prior to global buckling. Three major failure mechanisms were observed: facesheet cracking, facesheet buckling, and facesheet core debonding. Due to the catastrophic nature of the failure event, it is not possible to determine if these mechanisms evolved sequentially or simultaneously.
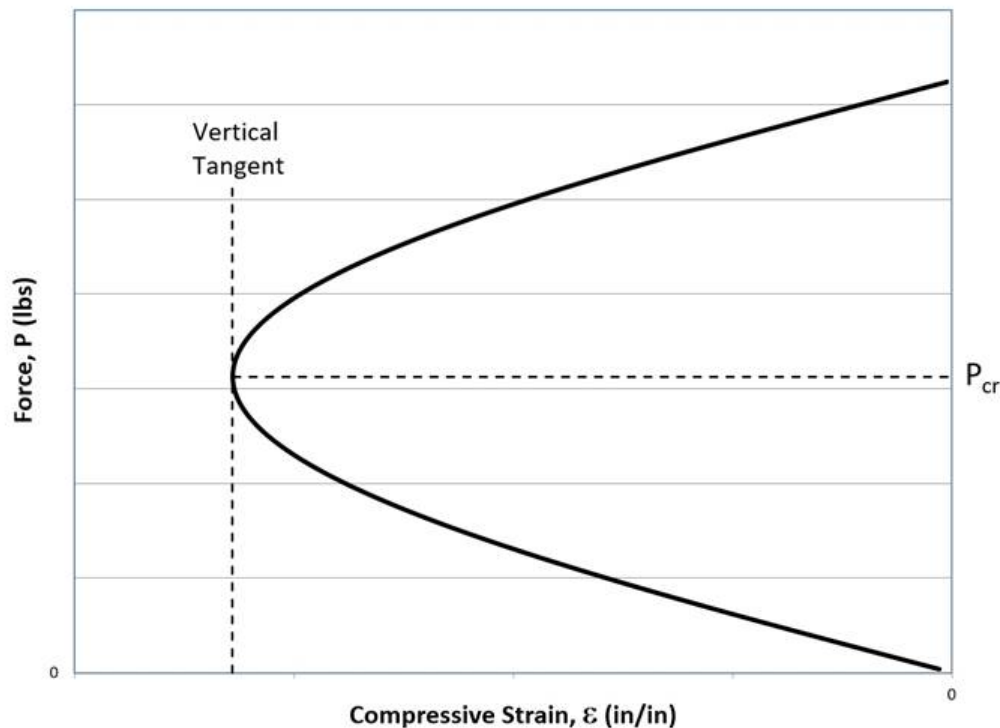

Figure 8.—Method for determining critical buckling load (P_{cr}) where ε is compressive strain.

Figure 9.—Failure mechanisms observed after catastrophic failure of panel immediately after onset of buckling. (a) Facesheet cracking. (b) Facesheet core disbonding. (c) Facesheet buckling, cracking, and core disbanding.

4.1   Linear Buckling Analysis

A linear buckling analysis was performed using Abaqus. Figure 10 shows the eigenvector plot when –0.243 in. was applied to the edge. The corresponding reaction load was 80,283 lb. Thus, the linear eigenvalue solution predicted a buckling load 25 percent higher than the test results. The significant error between the buckling load predicted using eigenvalue analysis and the experiment is attributed to the premature onset of failure. The other four panels that were analyzed exhibited much closer buckling loads, as compared to the experiment (Myers et al., 2013; Pineda et al., 2013; and Pineda et al., 2014). As mentioned before, the eigenvectors (shown in Figure 10) do not indicate the direction of buckling in a panel where there is a preferred direction, such as a curved panel. Thus, a nonlinear solution is necessary in order to predict the correct buckling direction.
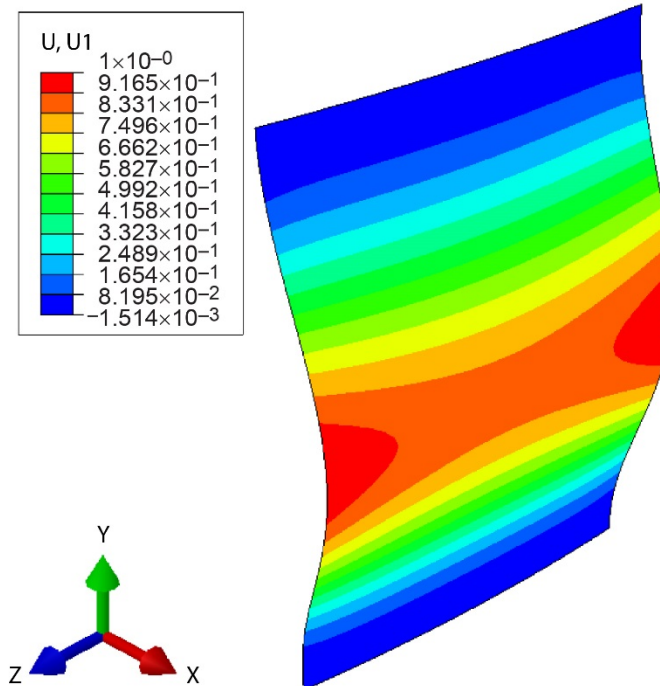
Figure 10.—Euler eigenvector buckling plot obtained from Abaqus.
U, U1 is out-of-plane displacement in x-direction from analysis.

4.2   Nonlinear Buckling Analysis

To obtain a more accurate prediction of the buckling load, a pretest, geometrically nonlinear analysis was executed using Abaqus. Figure 11 shows the load-deflection curves from the analysis as well as the experiment load cell data and measurements from three DCDTs. The buckling load predicted using linear eigenvalue analysis corresponds well with the maximum load of the load-deflection curve predicted with a geometrically nonlinear analysis. The stiffness obtained from the analysis was slightly lower than the test stiffness (see Table III). However it would appear from Figure 11 that, the stiffness of the panel calculated from the FEM analysis is higher than the test. This is because of some settling that is included in the experimental curve at very low loading.

Although no damage was detected in the specimen prior to testing using NDE, the nonlinearity in the experimental load-deflection response and the fact that the panel failed before global buckling may be evidence that there might have been some undetected damage and/or other imperfections in the panel that resulted in the large discrepancy between the buckling load prediction obtained from the nonlinear analysis and the experimental data. As with the eigenvalue buckling load predictions, the predictions for the buckling loads predicted using nonlinear analyses were far more accurate for the other four panels that were tested (Myers et al., 2013; Pineda et al., 2013; and Pineda et al., 2014).

Figure 12 shows the out-of-plane displacement contour plot and deformed shape obtained from analysis, at an applied edge displacement of –0.25 in., well into the postbuckled regime. This plot displays that panel buckling was predicted toward the O.D at a load of 77,312 lb, which is consistent with the buckling direction observed in the experiment. The out-of-plane displacement was monitored during the experiment using VIC and the VIC contour of the I.D. surface and is presented in Figure 12 at a load of 68,178 lb, also in the postbuckled regime, showing displacement also toward the O.D.
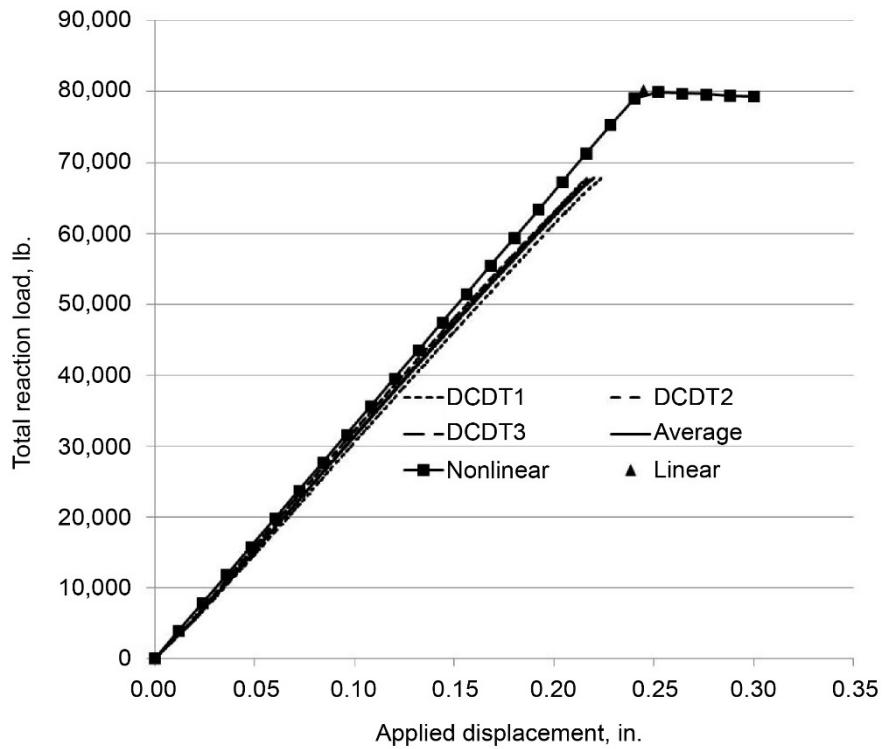
Figure 11.—Total reaction load versus end shortening for all analyses. Where DCDT is direct-current displacement transducer.

TABLE III.—TANGENT SLOPES OF CURVES IN FIGURE 11
AT AN END SHORTENING OF 0.1 in.

Curve	Slope
Nonlinear, ksi/in..318.1	
DCDT1[a], ksi/in 329.7	
DCDT2, ksi/in..319.4	
DCDT3, ksi/in..328.7	
DCDT specified average, ksi/in 326.0	

[a]Direct-current displacement transducer.
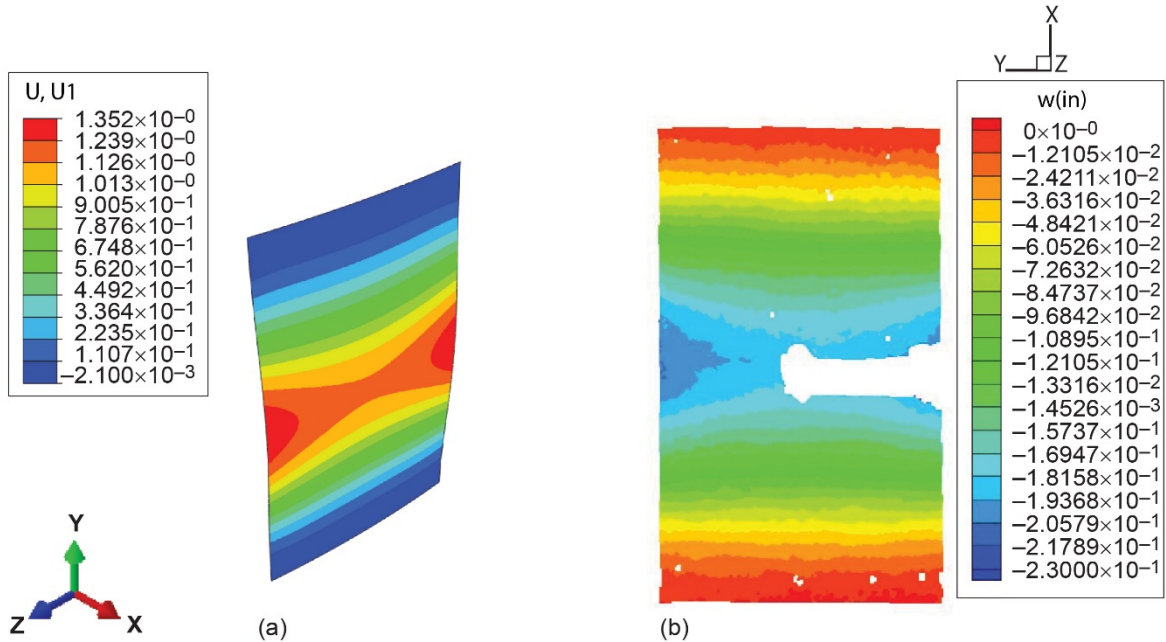
Figure 12.—Out-of-plane panel displacement from finite element method (FEM) and experiment. (a) FEM contour of out-of plane displacement at 77,312 lb, indicating buckling toward O.D. (b) Out-of-plane displacement visual image correlation data of I.D. at 68,178 lb (load), indicating buckling toward O.D. Note that coordiante axes for plots are different. U, U1 and w(in) are the out-of plane displacements in the x-direction from the analysis and experiment, respectively.

In previous studies with similar panels, the geometric imperfections in the panel were enough to drive the buckling of the panel away from the direction of major curvature, toward the I.D., and this was predicted through inclusion of the geometric imperfections in the models (Myers et al., 2013; Pineda et al., 2013; and Pineda et al., 2014). For the current panel (Panel D), the panel buckled toward the O.D., as indicated by Figure 12. Here, the analysis was able to predict that the degree of geometric imperfections was not enough to drive the buckling mode in the direction opposite of the major curvature. That is, the analysis results predicted the test results.

The buckling load determined using the strains at gages 1 and 2 was 76,266 lb. Predicted loads corresponding to all strain gage locations are tabulated with the experimental values in Table IV. Figure 13 to Figure 21 show load versus strain gage data for all gages from the experiment and the nonlinear analysis. The analysis and experimental data agree qualitatively. Figure 13 and Figure 14 show the strain gage measurements in the upper corners. Figure 15 shows the strain gage measurements at a panel inflection point at the ¾ panel length location. Figure 16 to Figure 18 show that at the horizontal center of the panel, the O.D. panel strain goes into compression up to buckling and then starts to reverse as the load increases during post-buckling, which is representative of buckling towards the O.D. The results from Figure 19, the lower inflection or ¼ length location, match the results from Figure 15, while the results from Figure 20 and Figure 21 match the results from Figure 13 and Figure 14, respectively. The strain reversal in Figures 13, 14, 20, and 21 occurs in the even gages which indicates local buckling towards the I.D. This is because the curvature of the panel combined with the constraints of the B.C.s will not allow for local buckling towards the O.D. in these regions. This is also observed in the analysis displacement contour of the post-buckled panel in Figure 12. The area near the constrained boundaries display a negative (towards I.D.) displacement magnitude. The error in the nonlinear analysis ranges from ~17 to 19 percent (Table IV). Again, the large error is attributed to premature failure of the test specimen.

TABLE IV.—APPROXIMATE TEST AND ANALYSIS
PREDICTION BUCKLING LOADS. SEE FIGURE 4
FOR GAGE LOCATIONS ON PANEL

Gage	Test, lb	Analysis, lb	Error, percent
Nos. 1, 2	63,947	76,266	19.2
Nos. 3, 4	64,483	76,266	18.3
Nos. 7, 8	64,442	76,500	18.7
Nos. 9, 10	65,637	77,238	17.7
Nos. 11, 12	64,813	77,238	19.1
Nos. 13, 14	65,534	77,238	17.9
Nos. 17, 18	64,442	76,266	18.3
Nos. 19, 20	64,442	76,266	18.3
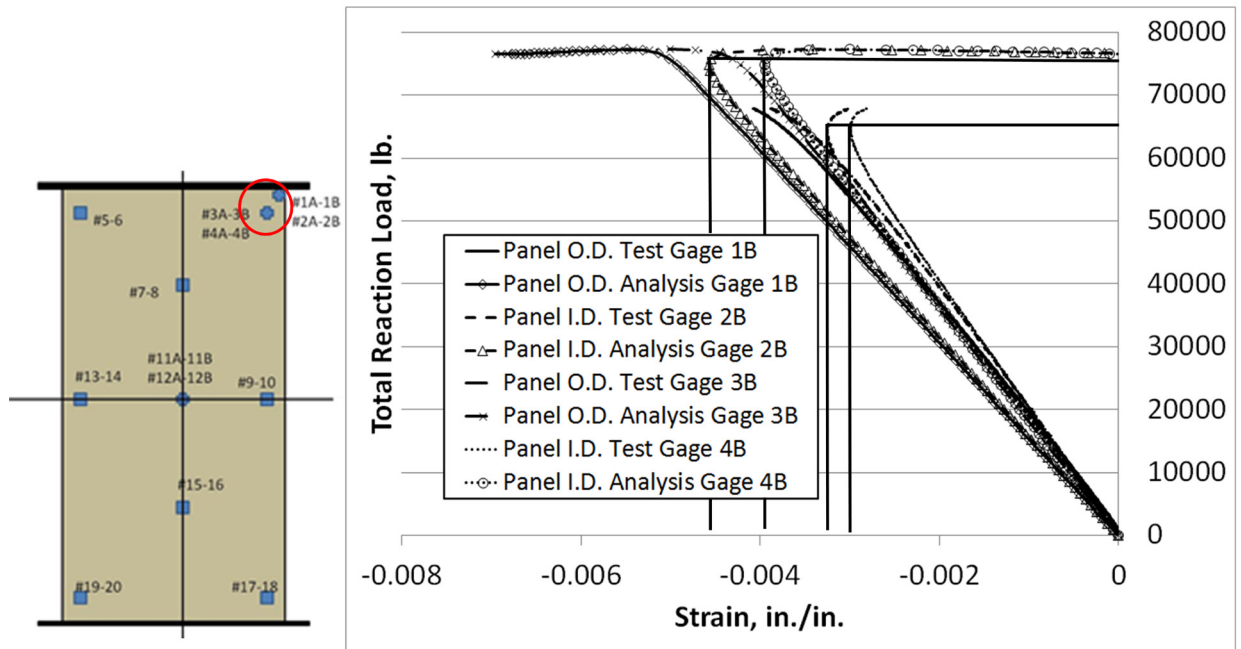
Figure 13.—Strain gage numbers 1 to 4 testing and analysis. (a) Strain gage locations, upper right corner of panel (see Figure 4). (b) Load versus strain plot.
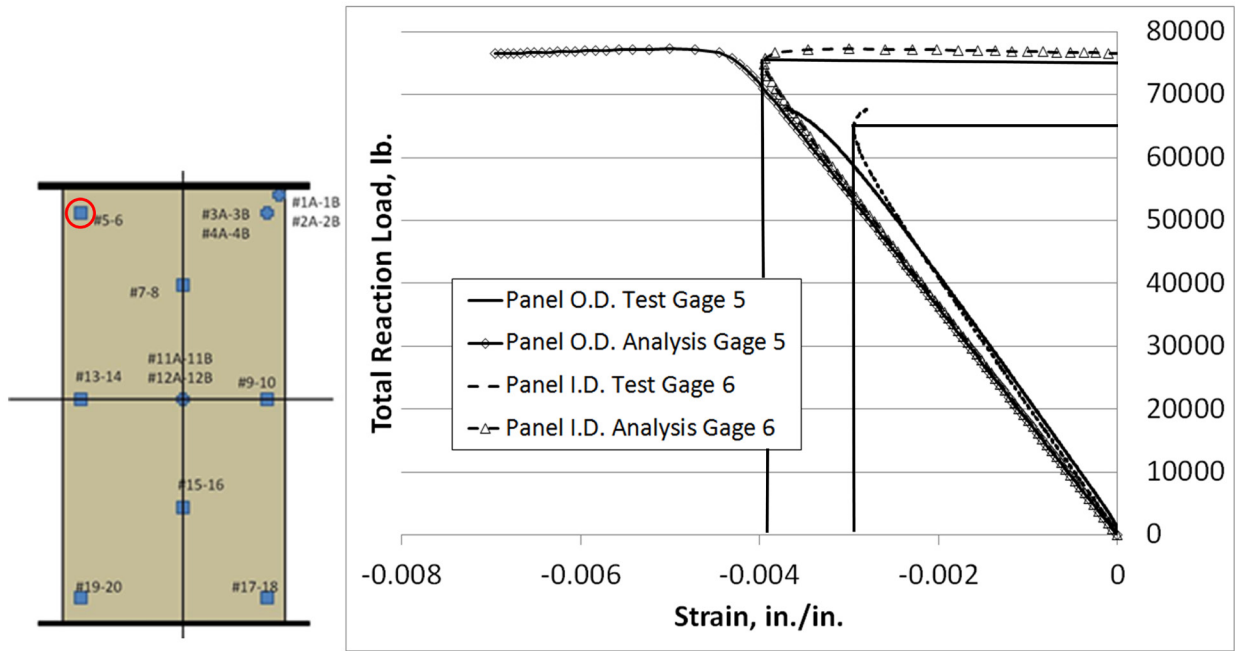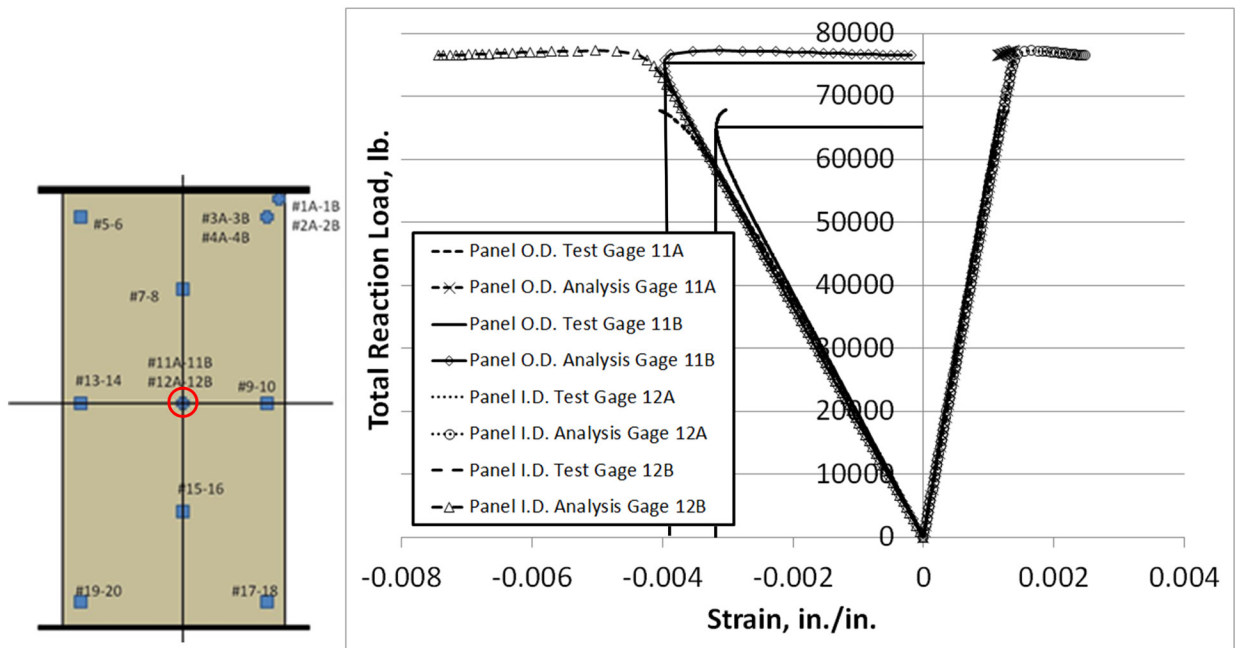
Figure 14.—Strain gage numbers 5 and 6 testing and analysis. (a) Strain gage locations, upper left corner of panel (see Figure 4). (b) Load versus strain plot.
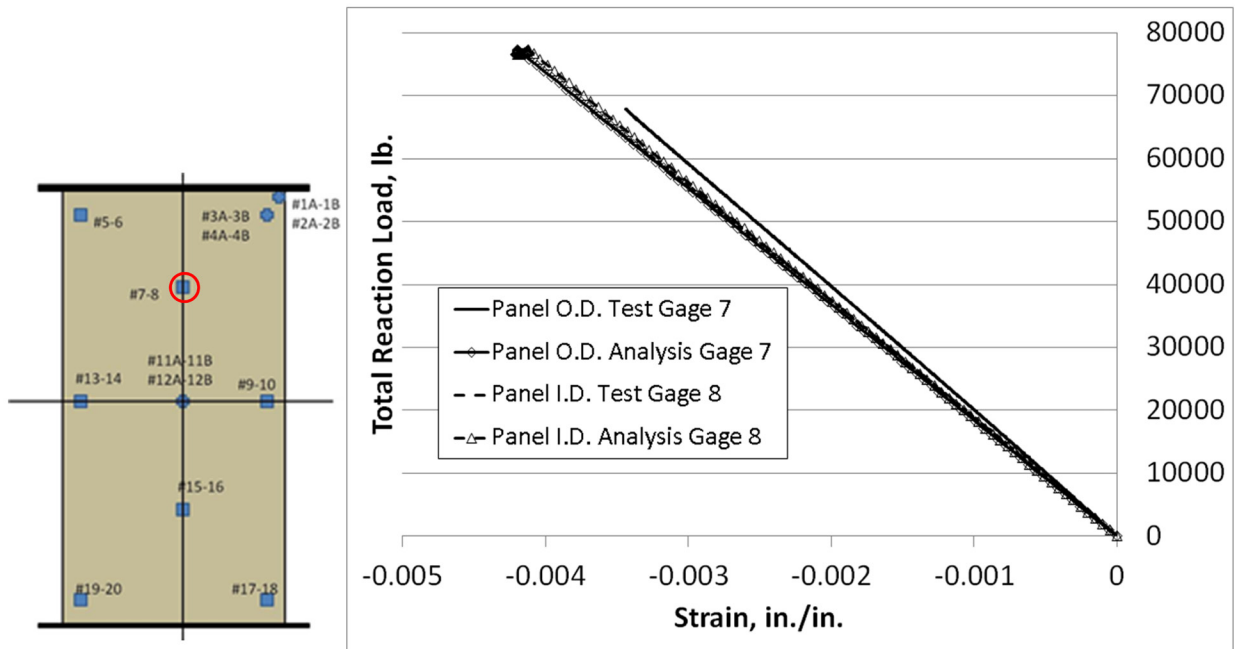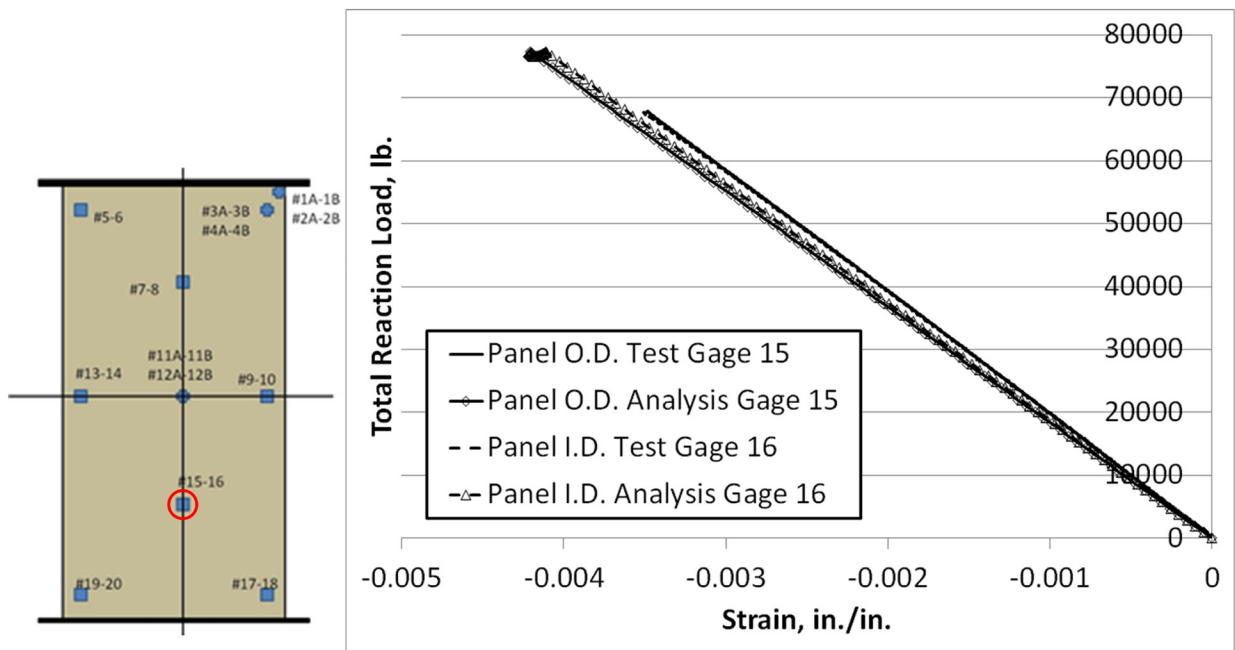

Figure 15.—Strain gage numbers 7 and 8 testing and analysis. (a) Strain gage location, panel inflection point at ¾ length (see Figure 4). (b) Load and strain plot.
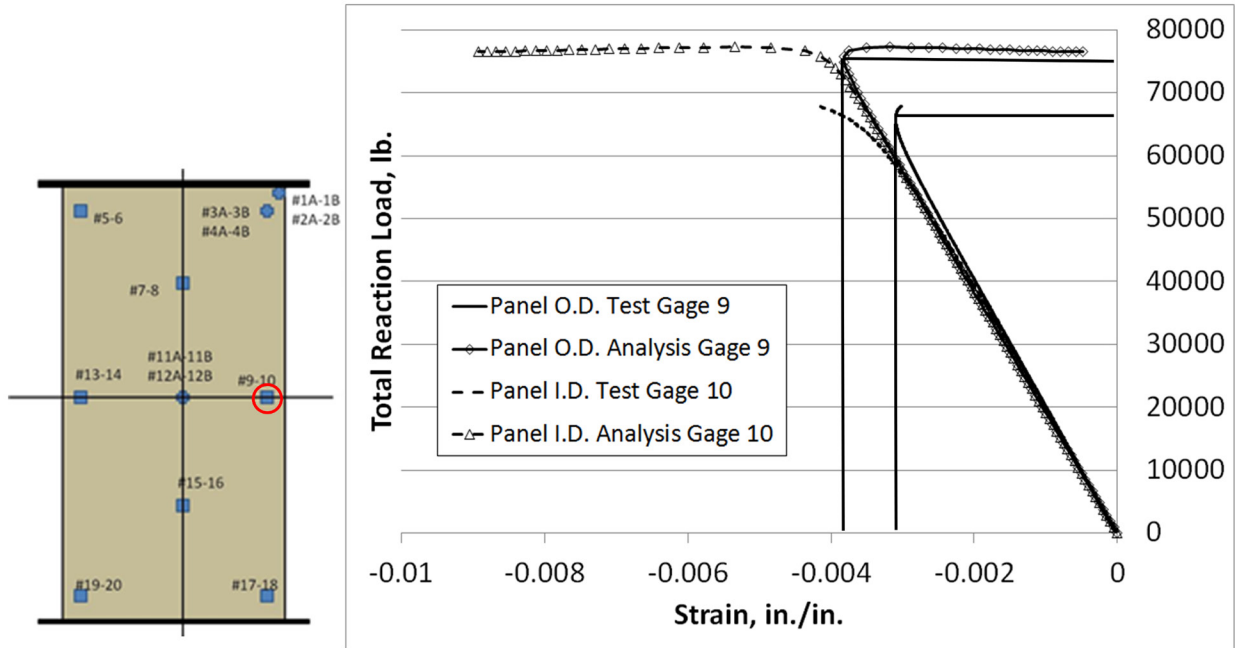
Figure 16.—Strain gage numbers 9 and 10 testing and analysis. (a) Strain gage locations, center of panel (right side) (see Figure 4). (b) Load versus strain plot.

Figure 17.—Strain gage numbers 11 and 12 testing and analysis. (a) Strain gage locations, center of panel (see Figure 4). (b) Load versus strain plot. The positive strain comes from the even "A" strain gages which measure circumferential strain.
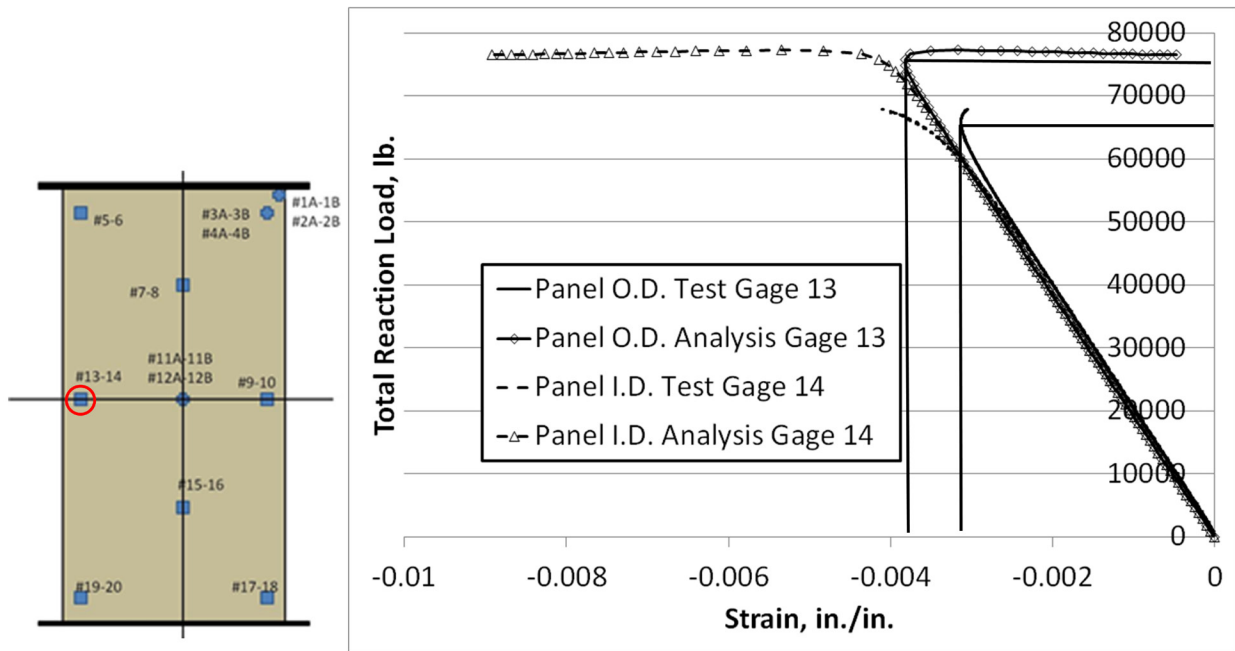
Figure 18.—Strain gage numbers 13 and 14 analysis and testing. (a) Strain gage locations, center of panel (left side) (see Figure 4). (b) Load versus strain plot.

Figure 19.—Strain gage numbers 15 and 16 analysis and testing. (a) Strain gage locations, panel inflection point at ¼ length (see Figure 4). (b) Load versus strain plot.
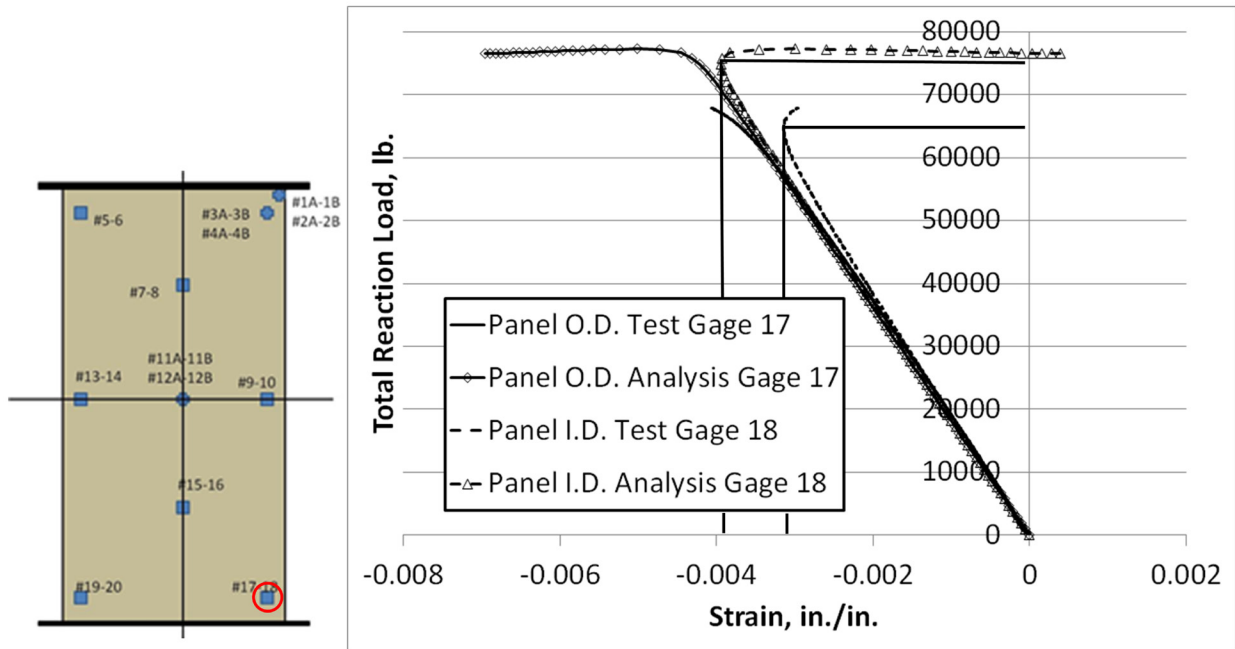
Figure 20.—Strain gage numbers 17 and 18 analysis and testing. (a) Strain gage locations, lower right (see Figure 4). (b) Load versus strain plot.
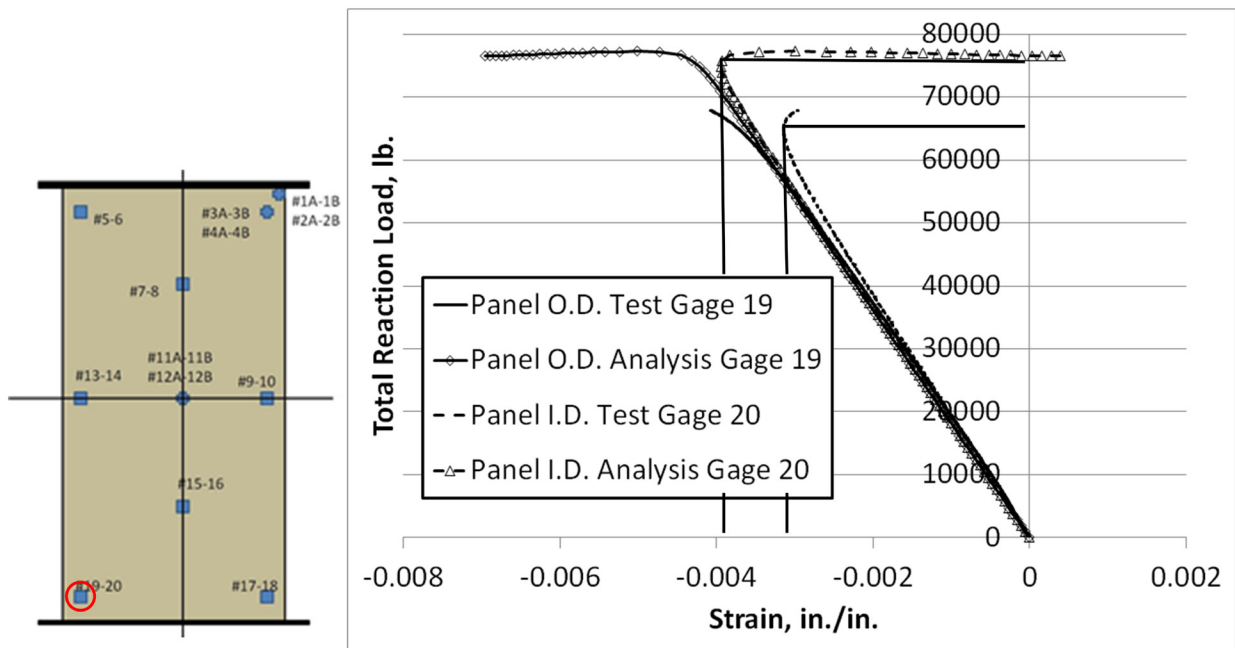
Figure 21.—Strain gage numbers 19 and 20 analysis and testing. (a) Strain gage locations, lower left (see Figure 4). (b) Load versus strain plot.

Figure 22 shows that the postbuckled, in-plane displacement photogrammetry results compared well qualitatively with the analytical predictions. Since shell elements were used in the analysis, the nodal displacements do not vary on the O.D. and I.D. surfaces, whereas, the test results showed there is some slight variation in displacement for the I.D. and O.D. surfaces due to the finite width of the panel. Figure 23 shows that the postbuckled, out-of-plane, displacement also compared well qualitatively with the analytical predictions.
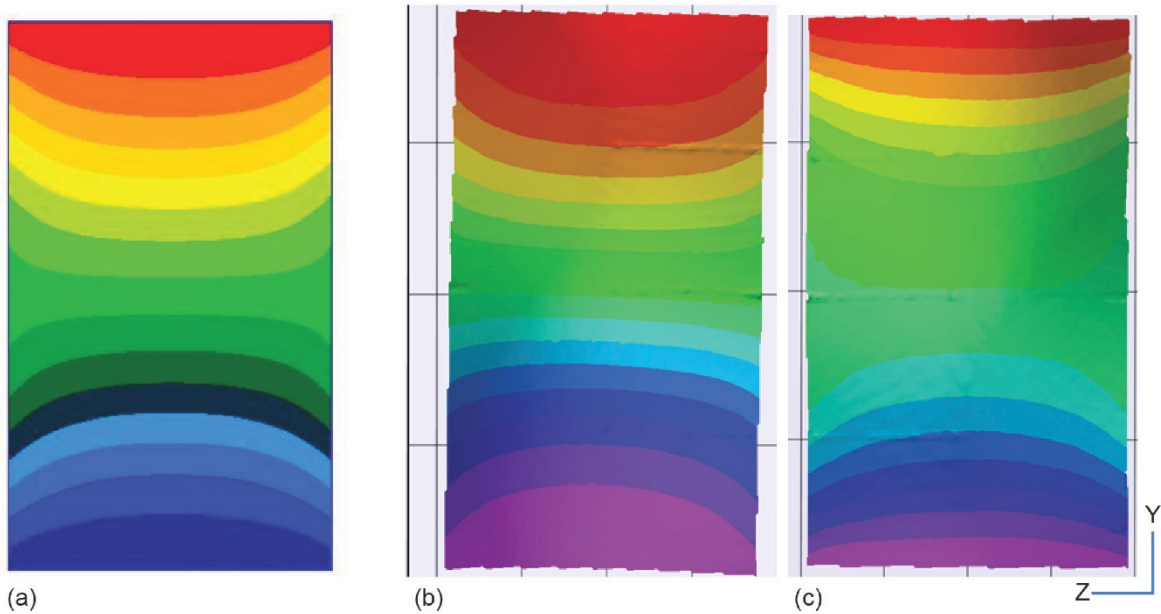

Figure 22.—Postbuckling Y (in-plane) displacement comparison. (a) Analytical prediction at neutral surface for two-dimensional model. (b) Photogrammetric results of O.D. surface. (c) Photogrammetric results of I.D. surface.
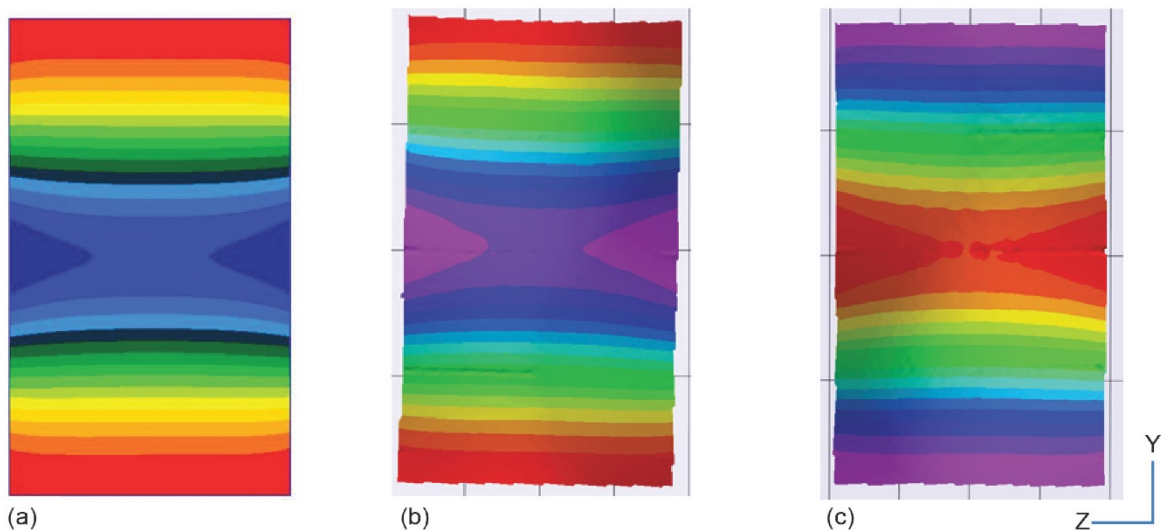

Figure 23.—Postbuckling X (out-of-plane) displacement comparison. (a) Analytical prediction at neutral surface for two-dimensional model. (b) Photogrammetric results of O.D. surface. (c) Photogrammetric results of I.D. surface.

For the O.D. surface, Figure 24 show that the postbuckled, minimum principal strain test results compared well qualitatively with the analytical predictions. For the I.D. surface, Figure 25 shows that the minimum principal strain also compared well. Figure 26 and Figure 27 show the maximum principal strain comparison for the O.D. and I.D. Again, the analysis compares well with the experimental results
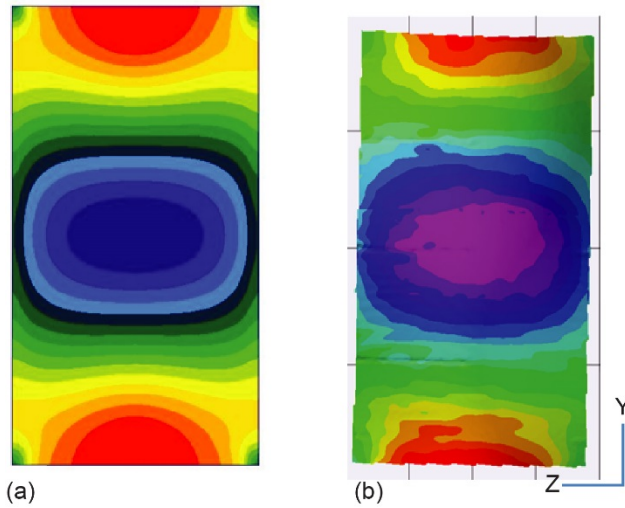

Figure 24.—Postbuckling O.D. minimum principal (Y) strain comparison. (a) Analytical predictions. (b) Photogrammetric results.
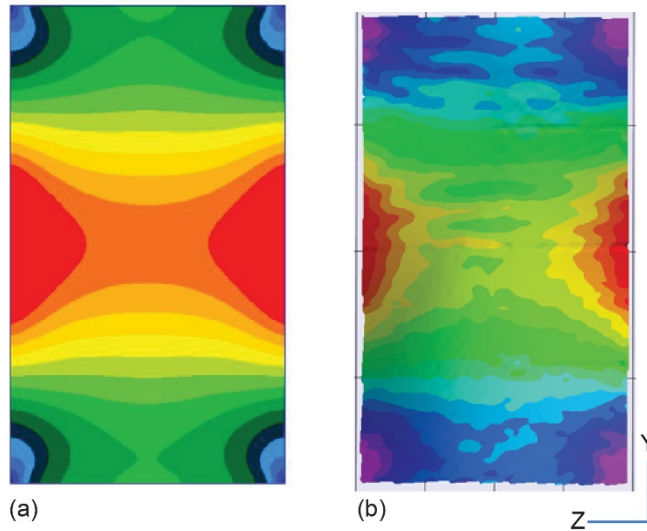

Figure 25.—Postbuckling I.D. minimum principal (Y) strain comparison. (a) Analytical predictions. (b) Photogrammetric results.
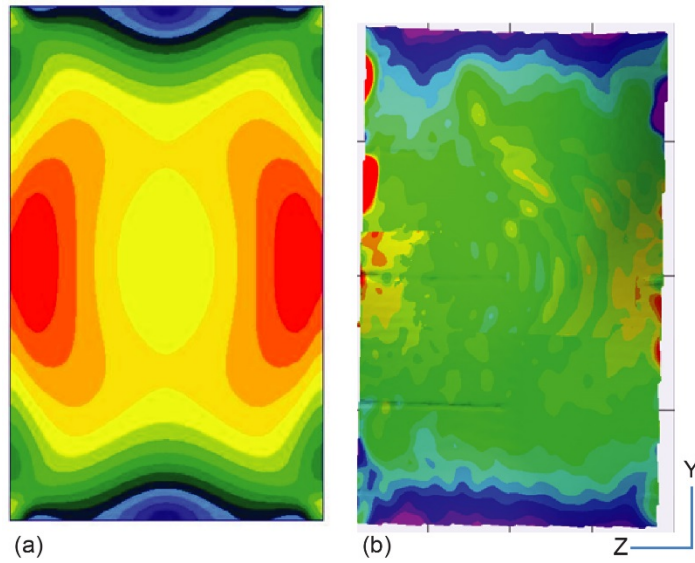
Figure 26.—Postbuckling O.D. maximum principal (Z) strain comparison. (a) Analytical predictions. (b) Photogrammetric results.
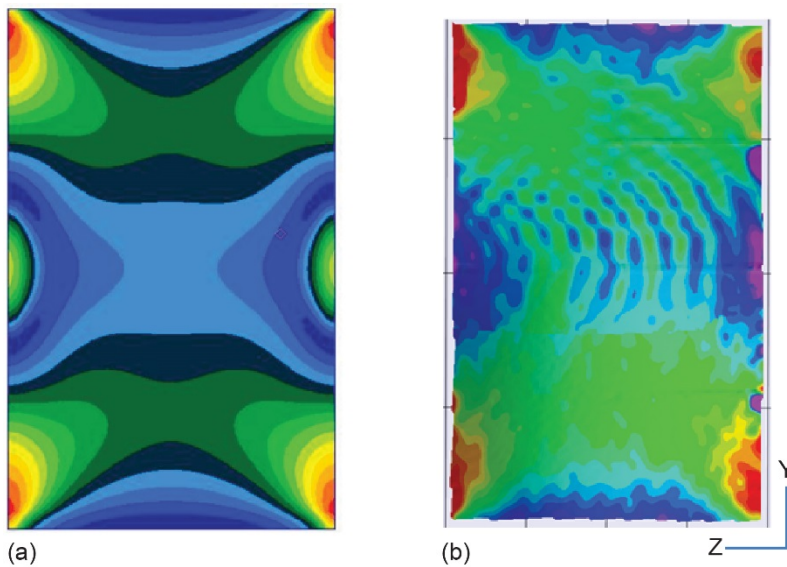

Figure 27.—Postbuckling I.D. maximum principal (Z) strain comparison. (a) Analytical predictions. (b) Photogrammetric results.

4.3   Strength Analysis at Buckling Load

In a separate linear static analysis, the panel was loaded up to the buckling load (determined from the nonlinear static analysis) using MSC Nastran SOL 101. This analysis was performed to confirm that panel failure was stiffness driven (i.e., the panel would be expected to buckle before it failed in strength). Figure 28 shows the strength ratio plot for the panel at the buckling load. The strength ratio is the local stress versus the allowable, and it incorporates one of three multiaxial failure criteria: Tsai-Wu, Tsai-Hill, or Hoffman (Jones, 1999). Figure 28 shows the lowest strength ratio among the three criteria and all facesheet plies, for each element. The analysis showed that a load 2.15 times greater than the buckling load would be required to fail the panel in strength, indicating that the panel is indeed stiffness driven.

4.4   ANSYS® Three-Dimensional Finite Element Model

The 3- by 5-ft arc-segment sandwich panel was investigated using two different ANSYS® finite element models. The first model was a two-dimensional layered structural shell element from which the results have been presented earlier. The second model was a three-dimensional layered structural solid-shell element model in which the test fixtures were also included. In ANSYS®, the two-dimensional layered shell element is called a SHELL281 finite element, and the three-dimensional solid-shell is called a SOLSH190 finite element. These finite element types are shown in Figure 29. A shell element is similar to a Nastran quad element, while the solid-shell is similar to a brick element. The SOLSH190 element can be used to model shell structures with a wide range of thickness from thin to moderately thick. Furthermore, the SOLSH190 element formulation permits small thickness to length ratios without producing errors due to large aspect ratios. The thickness between the nodes must equal the sum of the individual layer thicknesses. Otherwise, ANSYS® will scale the individual layer thicknesses to fit the actual element thickness.
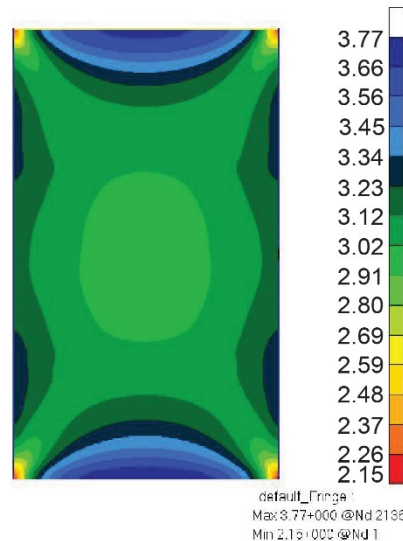

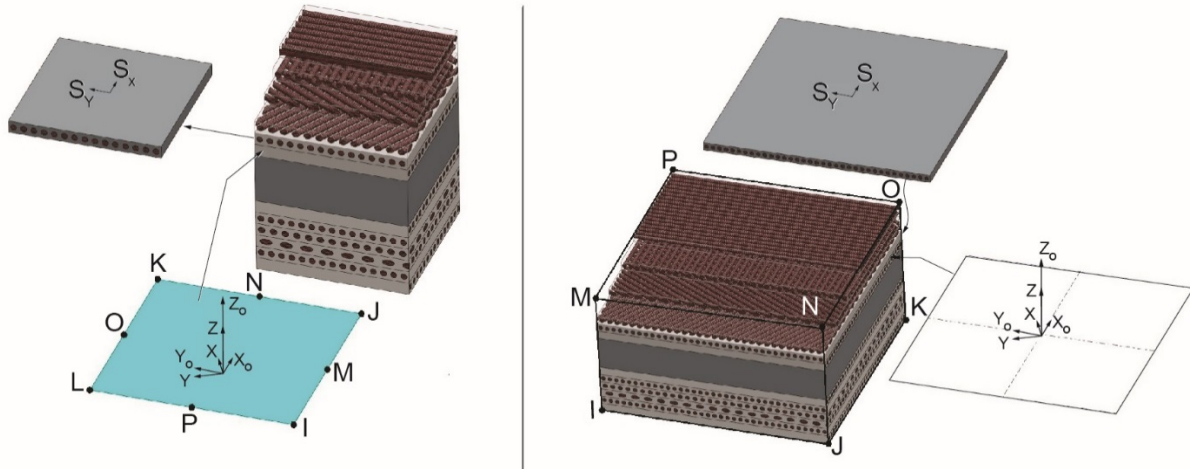Figure 28.—Strength ratio plot at buckling load.

Figure 29.—ANSYS® two-dimensional shell versus three-dimensional solid-shell (brick) finite elements. (a) SHELL281: two-dimensional eight-node structural shell with layered composite capability. (b) SOLSH190: three-dimensional eight-node structural solid shell with layered composite capability. Where I, J, K, L, M, N, O, and P represent elemental node numbers.

TABLE V.—ELASTIC PROPERTIES FOR
UNISORB® V-100 POTTING COMPOUND

Property	Value
E, ksi	436
ν	0.35

Figure 30 shows the model of the test panel geometry with the end plates. For clarity, the finite element edges are suppressed. The panel was modeled as 62 in. tall, including the 1-in. aluminum end plates and 36 in. width along the chord. The top and bottom 1 in. portions of the panel were supported in the potting material and end plates. Figure 31 shows the slot in the end plate shaped like the arc segment test specimen model. The end of the specimen model is centered in the slot, and the 0.5-in. space around the specimen is filled with solid elements modeling the UNISORB® V-100 potting compound with the elastic properties given in Table V. Each color represents a different material assignment: cyan for the T40-800B/5320-1 facesheets, purple for the honeycomb core, red for the potting compound, and orange for the aluminum end plates.

The solid model was generated using a script file containing ANSYS® preprocessing, finite element solution, and postprocessing commands in the ANSYS® Parametric Design Language (APDL) (ANSYS®, 2011). The basic geometry, ply-stacking sequence, material properties, and geometric imperfections were defined using parameters. The script file can generate the finite element model, perform each analysis in sequence, and process the results in tabular or graphic format.

As shown in Figure 32, the stacking sequence of the facesheets was $[60°/–60°/0°]_s$ with 0.0053-in.-thick plies. Again, the T40-800B/5320-1 elastic properties came from test data. Some material data was not available, so IM7/977-3 data was used where T40-800B/5320-1 data was not available. Since IM7/977-3 elastic properties and B-basis allowables were obtained from the Orion materials database, they are not listed due to ITAR restrictions (Lockheed Martin, 2010).   The aluminum (5052-T6 alloy) honeycomb properties were obtained from commercially available literature (Hexcel®) . Unlike the HyperSizer properties, the honeycomb in-plane longitudinal and transverse moduli (E_1 and E_2) were kept at 21.28 psi, and the in-plane shear modulus (G_{12}) was kept at 5.32 psi in the ANSYS® models (Table VI). The honeycomb normal (out-of-plane) modulus (E_3) was also kept at 75 ksi.
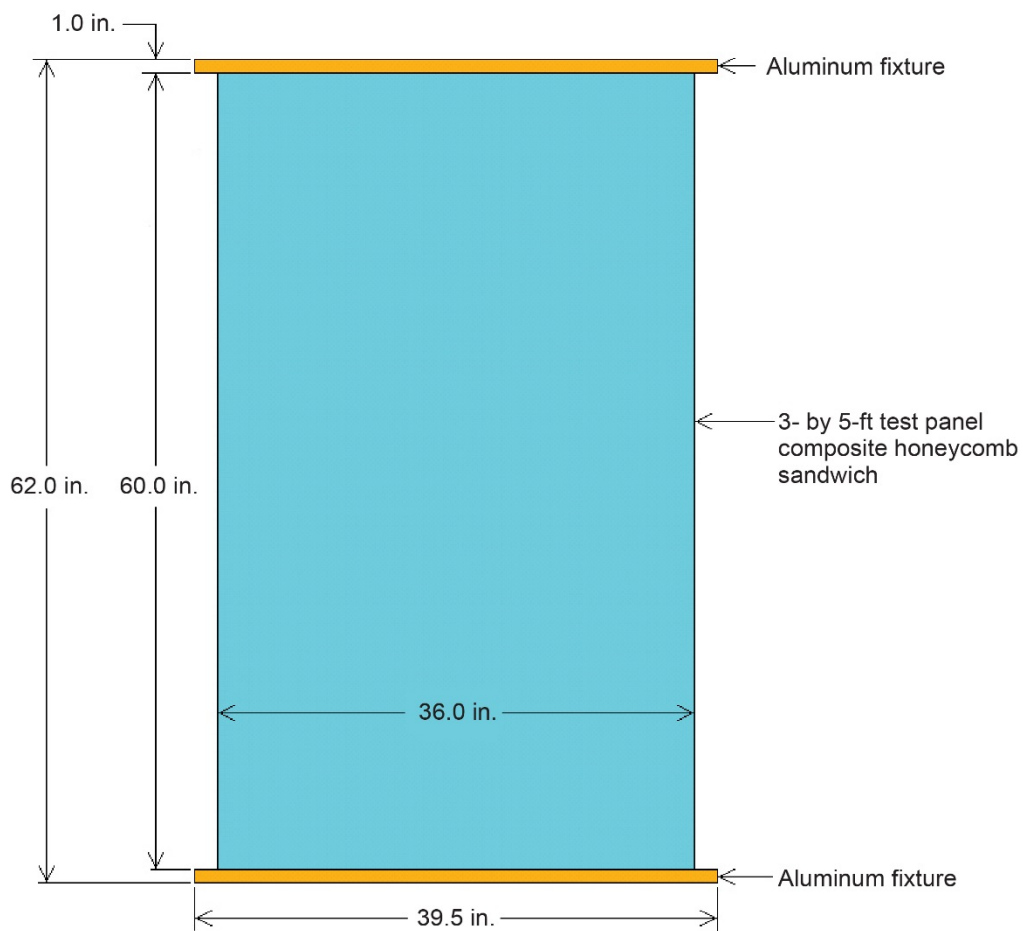
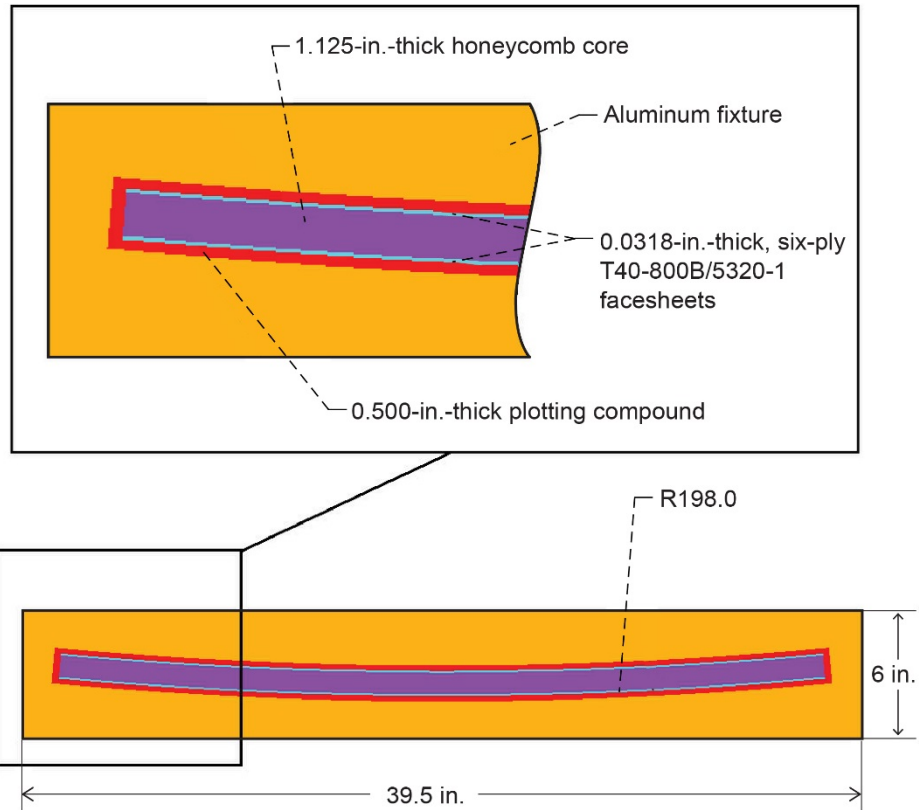Figure 30.—3- by 5-ft arc-segment test panel configuration.

Figure 31.—Six-ply, 3- by 5-ft arc segment test panel and test fixture end view.
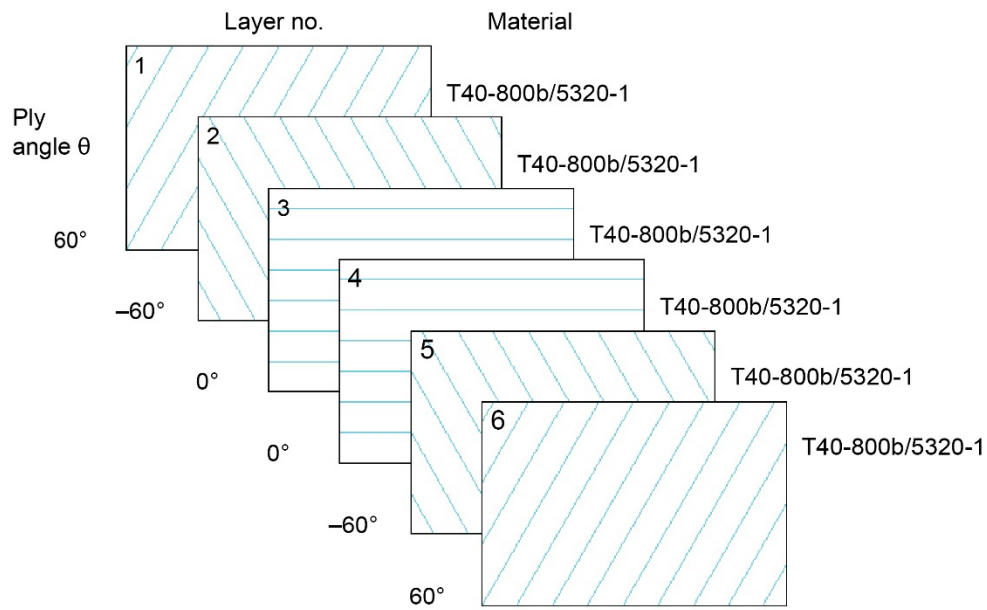

Figure 32.—Facesheet six-ply T40-800B/5320-1 stacking sequence.

TABLE VI.—ANSYS® MODEL, Al HONEYCOMB MATERIAL
PROPERTIES, 3.1 pcf, 1/8 in.-5052-0.0007 THICKNESS

Property	Value
E_1, psi	21.28
E_2, psi	21.28
E_3, ksi	75.0
υ_{12}	0.333
υ_{23}	1×10^{-5}
υ_{13}	1×10^{-5}
G_{12}, psi	5.32
G_{13}, ksi	45.0
G_{23}, ksi	22.0
γ, lb•in³	0.00179
μ, pcf	3.1
F_{t1}, psi	215
F_{c1}, psi	215
F_{t2}, psi	215
F_{c2}, psi	215
F_{t3}, psi	130
F_{c3}, psi	300
F_{s12}, psi	90
F_{s23}, psi	90
F_{s13}, psi	90

The actual panel was secured between two loading platens, with the bottom end plate fixed on the loading platen. The top end plate moved with the top platen in the axial direction. Referring to Figure 33, all three displacements in the solid-shell finite element model were fixed along the bottom edge of the panel and end plate. The same boundary condition was applied to the top panel edge and top end plate, except a displacement was applied in the negative z-axis direction.

It has been shown in this paper that the initial geometric imperfections have an impact on the buckling load and direction. Intuitively, a curved panel is expected to buckle toward the O.D. This 3- by 5-ft arc segment test panel buckled toward the O.D. since the bow was not large enough to push it towards the I.D. Therefore, the initial imperfect geometry is important in a nonlinear buckling analysis (Hong and Jun, 1989). If the 3- by 5-ft panel is modeled as perfectly symmetric (i.e., in geometry and loading), nonlinear progressive collapse does not occur numerically in ANSYS®.

One way to introduce antisymmetry to the model is to apply small perturbations to the applied loads or enforced displacements. This method is not ideal, because it is difficult to determine how to redistribute the loads. Furthermore, varying the load across the top of the panel too drastically could change the problem completely. Another way to introduce antisymmetry is to superimpose small geometric imperfections (similar to those caused by manufacturing) on the model to trigger the buckling responses. One way to generate these imperfections is with pseudorandom shapes, where the coordinates of the nodes are slightly modified with random amplitudes. The disadvantage in using random imperfections is that they cannot be repeated, and the results would differ for each analysis of the same panel. An easier way to impose geometric imperfections on the finite element model is to employ the linear (Eigen) buckling mode shapes.
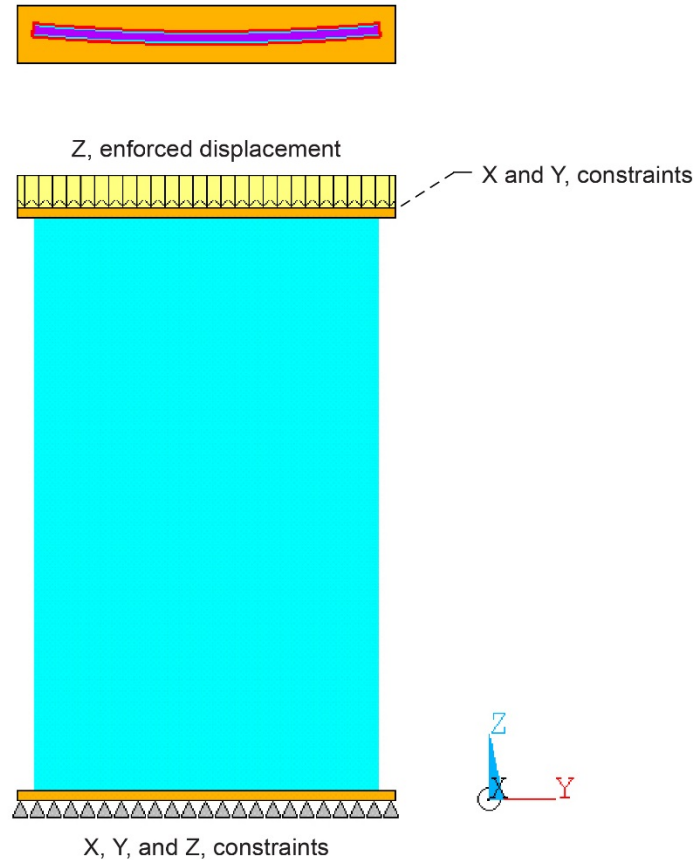
Figure 33.—ANSYS® solid model boundary conditions.

The buckling analysis of the 3- by 5-ft arc-segment panel requires several steps. First, the initial bow shape is imposed across the width of the panel model. The imperfections are obtained by running a preliminary linear buckling analysis, then updating the geometry of the finite element model to the deformed configuration. This technique is done by adding the displacements from the mode shapes multiplied by a scaling factor. The scaling factor is on the order of the manufacturing tolerances and initial bowed shape. A factor of +0.010 in. was chosen for the 3- by 5-ft panel. Furthermore, the scaling factor was positive to correspond to the direction of the initial bow shape. Applying a negative value would make the panel model buckle toward the I.D. The imperfections are also added as a sum of the first 10 mode shapes extracted in the preliminary linear buckling analysis as shown in Figure 34. The first 10 mode shapes were used to avoid any bias in the imperfections. Figure 35 shows the resulting geometry.

After the geometric imperfections are added to the finite element model, nonlinear buckling analysis is performed. In ANSYS®, nonlinear buckling analysis is a static analysis with large deflections active. The magnitude of the applied axial compression is extended beyond the first linear (Eigen) buckling mode. In this analysis, the compression was increased gradually using 50 small time increments to predict the critical buckling load.

Figure 36 shows the reaction load versus end compression for the linear and nonlinear shell and solid ANSYS® models and the actual test data of MTP-6010. The two linear buckling analyses and the nonlinear shell FEM analysis overpredicted the buckling load. The nonlinear solid FEM analysis is closest to the test result buckling load. In both nonlinear ANSYS® analyses, the panel stiffness was nearly the same.
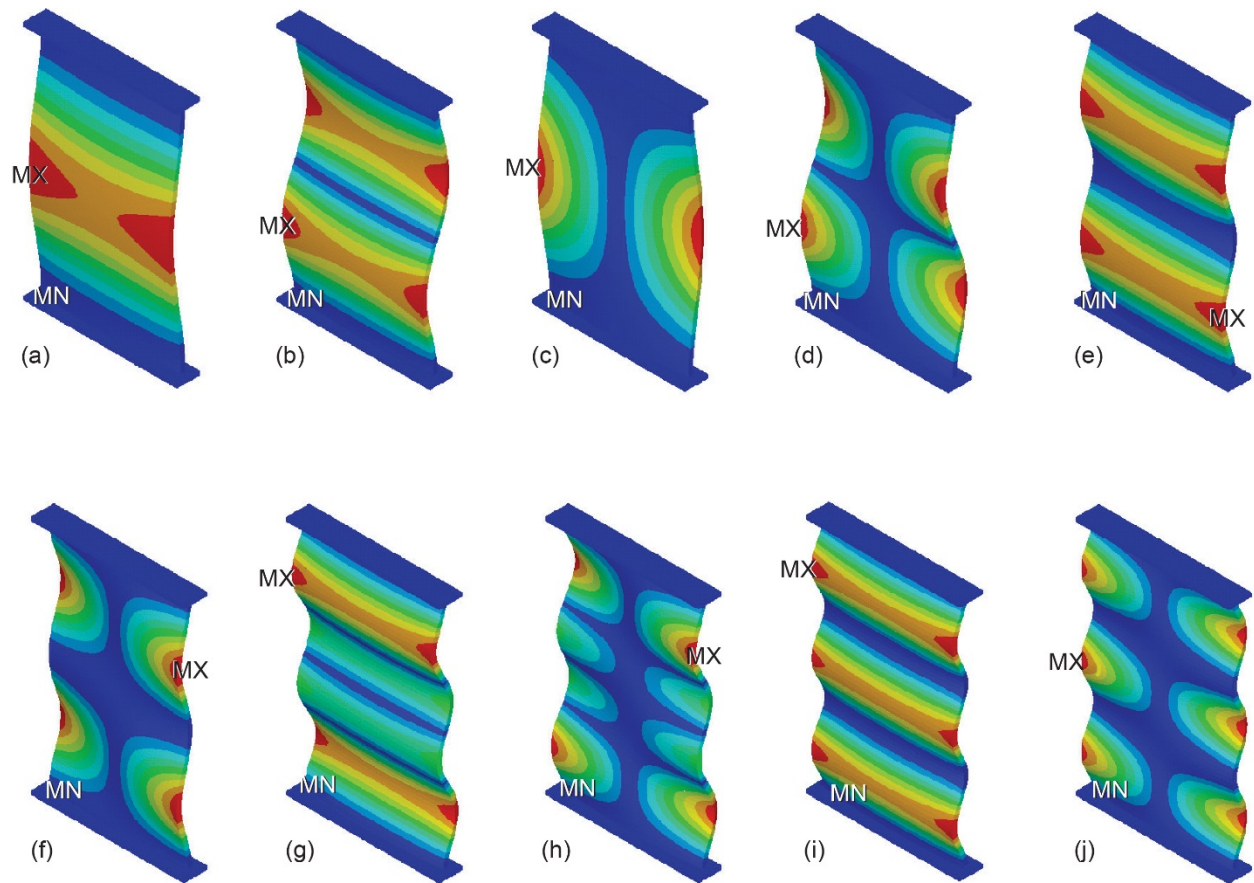
Figure 34.—First 10 linear buckling mode shapes for 3- by 5-ft panel with six-ply T40-800B/5320-1 facesheets. (a) Linear buckling mode 1, factor = 2.37986. (b) Linear buckling mode 2, factor = 4.52415. (c) Linear buckling mode 3, factor = 4.79078. (d) Linear buckling mode 4, factor = 6.76039. (e) Linear buckling mode 5, factor = 8.23791. (f) Linear buckling mode 6, factor = 10.1911. (g) Linear buckling mode 7, factor = 11.5403. (h) Linear buckling mode 8, factor = 13.3058. (i) Linear buckling mode 9, factor = 15.8211. (j) Linear buckling mode 10, factor = 17.2692. Where MX and MN show maximum and minimum displacement locations, respectively.
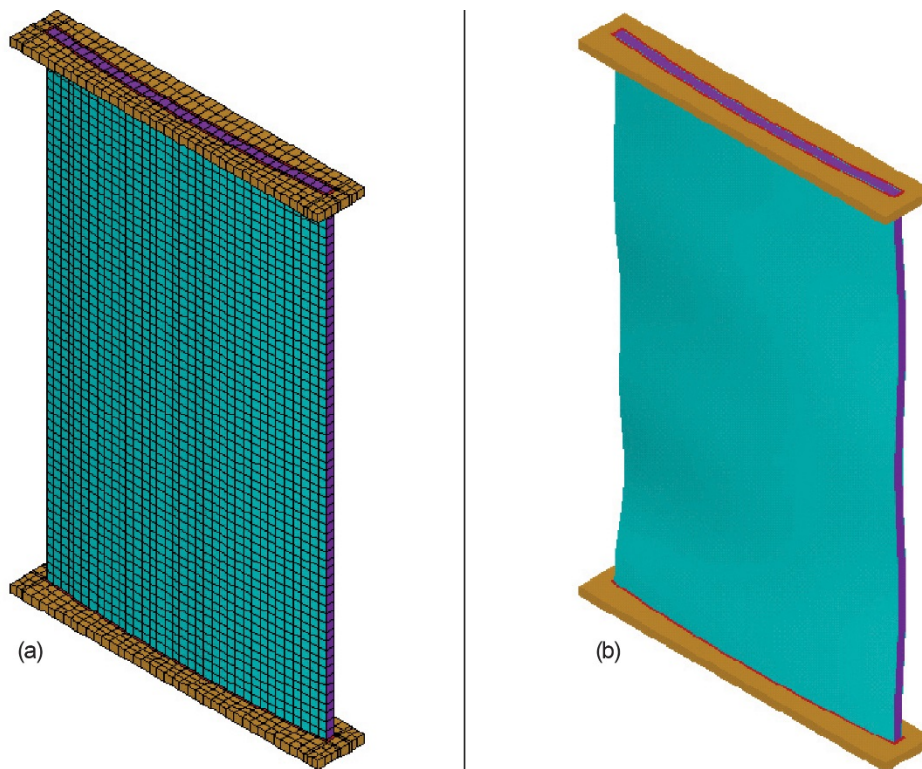
Figure 35.—Panel model with applied initial bowed shape and geometric imperfections (exaggerated). (a) Perfect geometry. (b) After initial bow shape and applied imperfections.
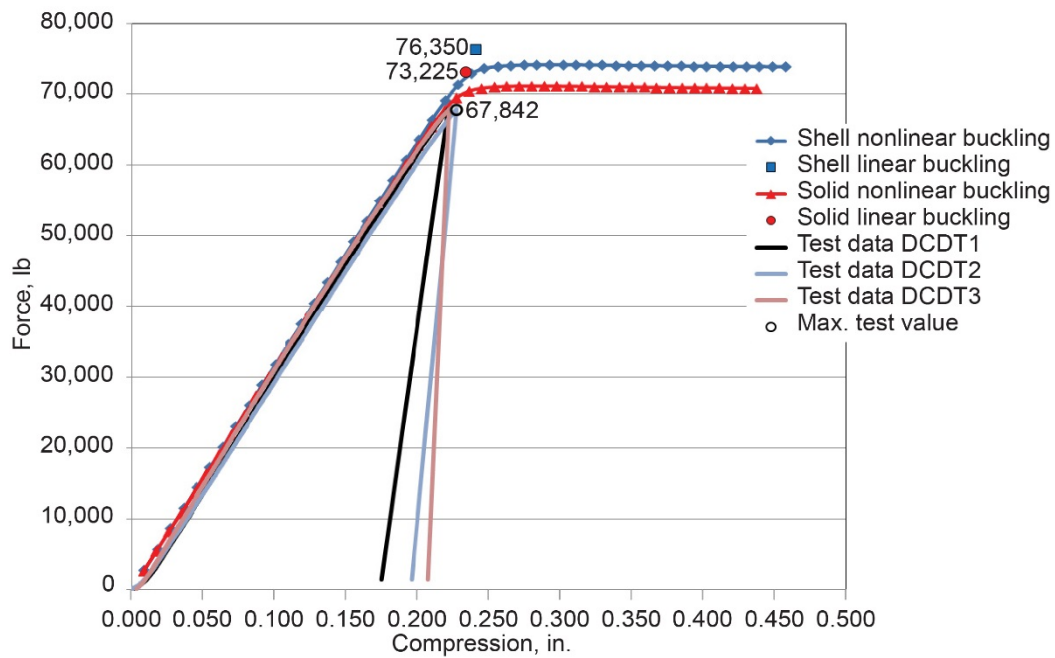

Figure 36.—Total reaction load versus end shortening for ANSYS® solid and shell finite element method of MTP–6010. Where DCDT is direct-current displacement transducer.
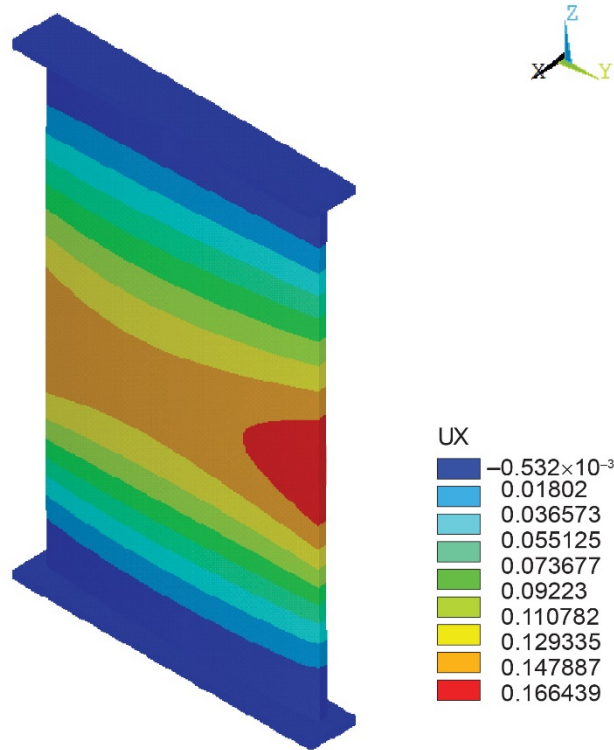
Figure 37.—ANSYS® solid finite element method global radial
displacement contour plot for MTP–6010 at 0.219-in. end
shortening with geometric imperfections and scale factor of
0.01. Where Ux is out-of-plane displacement in the x-
direction.

Figure 37 shows the panel radial displacement plot (radial component of the total displacement field) when –0.219 inches was applied to the top edge. As explained earlier, Figure 37 shows that the panel buckles in toward the O.D. or in the direction of the panel's outer surface. The plot also shows asymmetry in the radial displacements, which is also evident in the buckling predictions shown in Table VII. The asymmetry in the radial displacements of Figure 37 is due to the asymmetry in some of the linear buckling mode shapes (as shown in Figure 34), which were superimposed on the original geometry.

Figure 38 shows load versus strain plots for gages located in the center of the panel. On the O.D. side of the panel, the strain goes into compression up to buckling and then starts relieving itself as the load increases during postbuckling. On the I.D. side, the strain remains compressive (negative) and suddenly increases in magnitude during postbuckling. The analysis results for the ANSYS® shell and solid FEMs show the same trends in strain at that gage location.

Table VII shows that the first experimental strain reversal in the panel occurred at the location of gage numbers 1 and 2, located at the upper right corner of the panel, at a load of 63,947 lb. for MTP–6010. However, the three sets of gage locations across the middle of the panel (gage locations numbers 9 to 10, 11 to 12, and 13 to 14) show a difference of less than ±1 percent between the experimental and analytical data. Loads corresponding to all strain gage locations are tabulated with the experimental values in Table VII. Figure 39, Figure 40, and Figure 41 show that, in the corners, the axial I.D. (inner mold line (IML)) panel strains went into compression up to the onset buckling, after which the strain increment reverses and the axial strain is alleviated as the load increases during postbuckling. Figure 42 shows the strain gage measurements at a panel inflection point at the ¾ panel length location. Figure 43 to Figure 45 show that at the horizontal center of the panel, the axial O.D. (OML) panel strains went into compression up to the onset

buckling, after which the strain increment reverses and the axial strain is alleviated as the load increases during postbuckling. As pointed out earlier in this paper, this local behavior (observed both experimentally and numerically) is consistent as the panel buckled toward the O.D. Note that, since the major curvature of the panel is biased toward the O.D., the analysis would predict buckling toward the O.D. if no geometric imperfections, or bow, were introduced into the model. The results from Figure 46 at the lower inflection or ¼ length location match the results from Figure 42. The results in the lower corners from Figure 47 and Figure 48 match the results from the upper corners in Figure 39 and Figure 41, respectively. The error in the nonlinear analyses ranges from 0.20 to 2.56 percent for the MTP–6010 panel (Table VII), which was an improvement over the linear analyses and the analyses using Abaqus which were between 17 to 19 percent.

TABLE VII.—APPROXIMATE TEST AND ANALYSIS
PREDICTION BUCKLING LOADS FOR MTP–6010

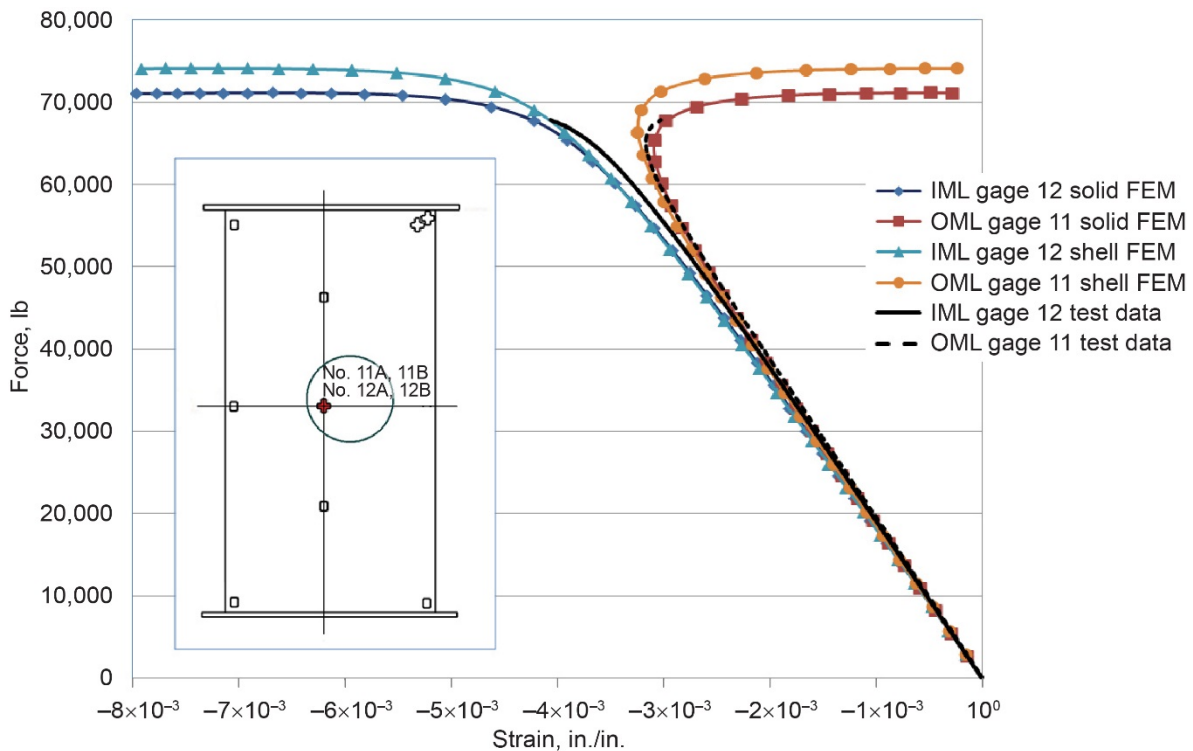| Gage	Test, lb	Analysis, lb	Error, percent
Nos. 1, 2	63,947	62,830	1.75
Nos. 3, 4	64,483	62,830	2.56
Nos. 5, 6	64,442	62,830	2.50
Nos. 9, 10	65,637	65,403	0.36
Nos. 11, 12	64,813	65,403	–0.91
Nos. 13, 14	65,534	65,403	0.20
Nos. 17, 18	64,442	62,830	2.50
Nos. 19, 20	64,442	62,830	2.50

Figure 38.—Load versus minimum principal strain plot for MTP–6010 at gage numbers 11 and 12. Where FEM is finite element method, IML is inner mold line, and OML is outer mold line.
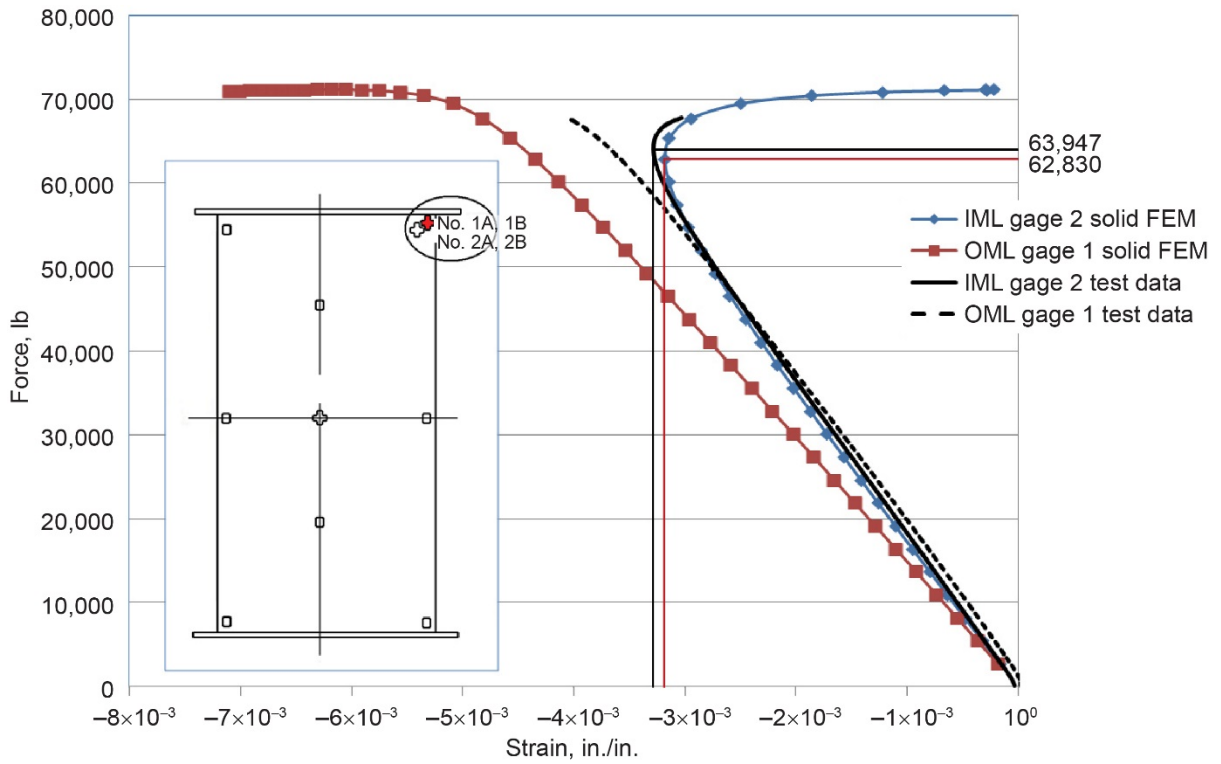
Figure 39.—Load versus minimum principal strain plot for gage numbers 1 and 2. Where FEM is finite element method, IML is inner mold line, and OML is outer mold line.

Figure 40.—Load versus minimum principal strain plot for gage numbers 3 and 4. Where FEM is finite element method, IML is inner mold line, and OML is outer mold line.
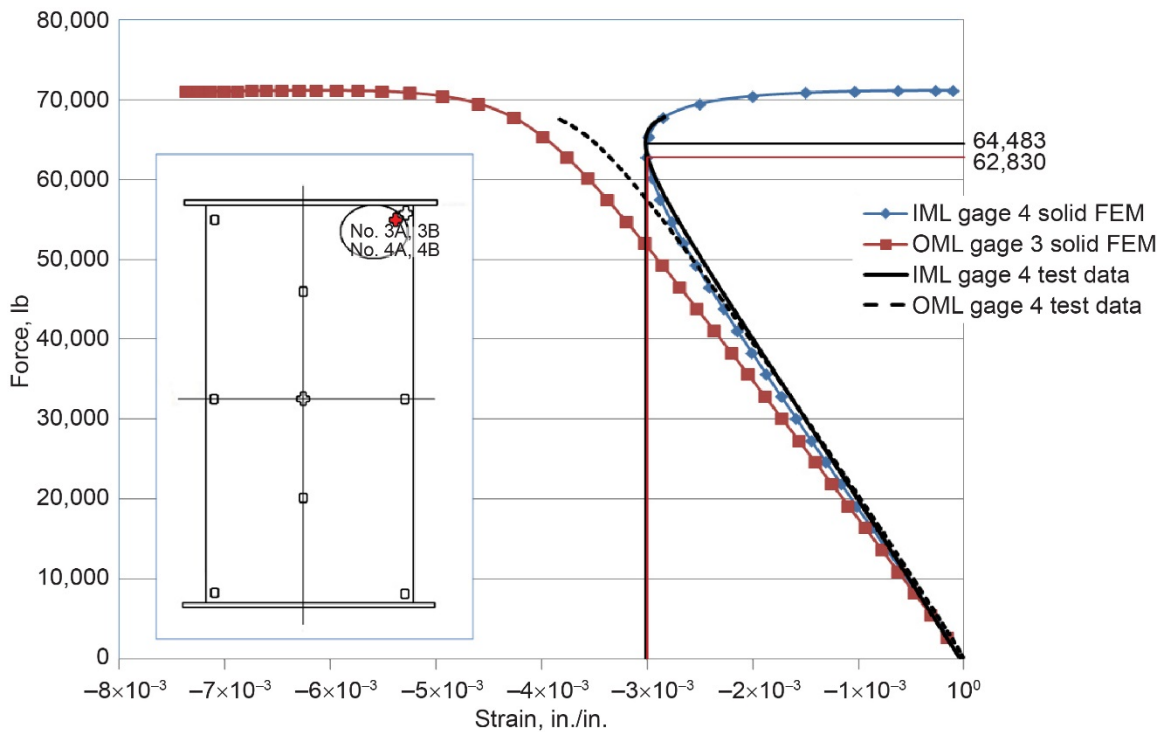
Figure 41.—Load versus minimum principal strain plot for gage numbers 5 and 6. Where FEM is finite element method, IML is inner mold line, and OML is outer mold line.

Figure 42.—Load versus minimum principal strain plot for gage numbers 7 and 8. Where FEM is finite element method, IML is inner mold line, and OML is outer mold line.

Figure 43.—Load versus minimum principal strain plot for gage numbers 9 and 10. Where FEM is finite element method, IML is inner mold line, and OML is outer mold line.
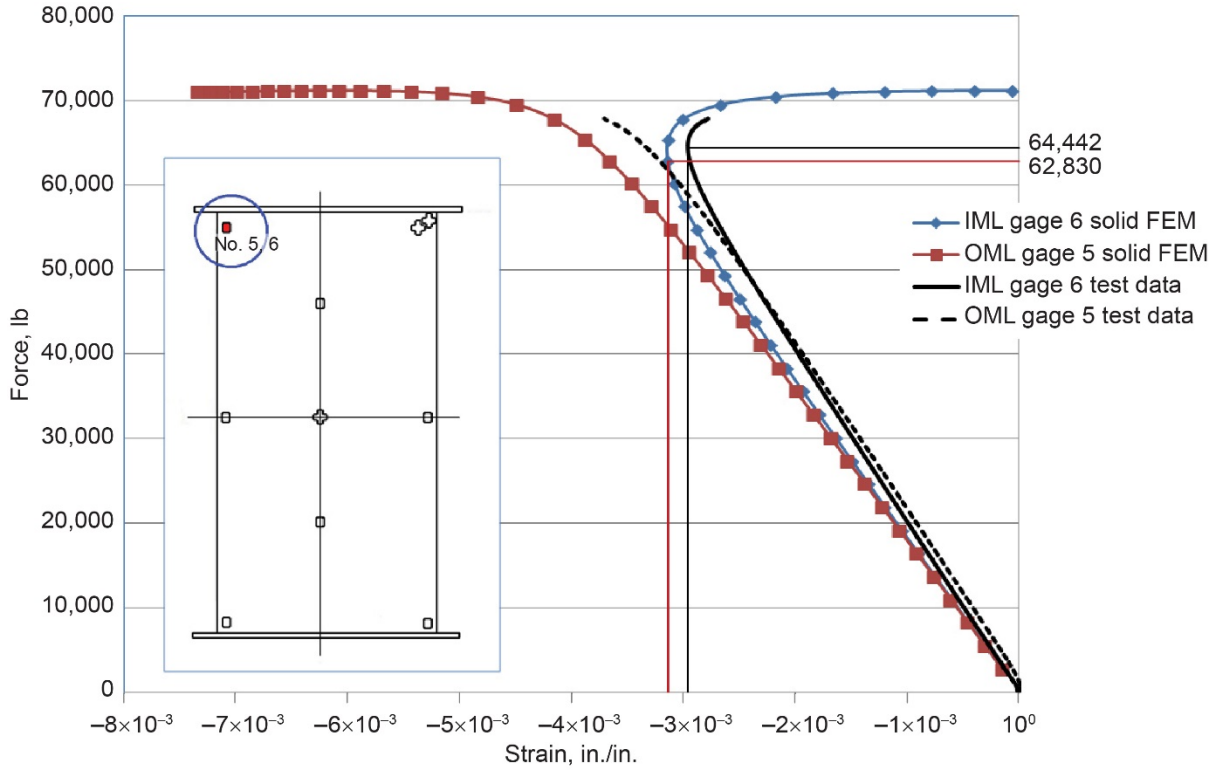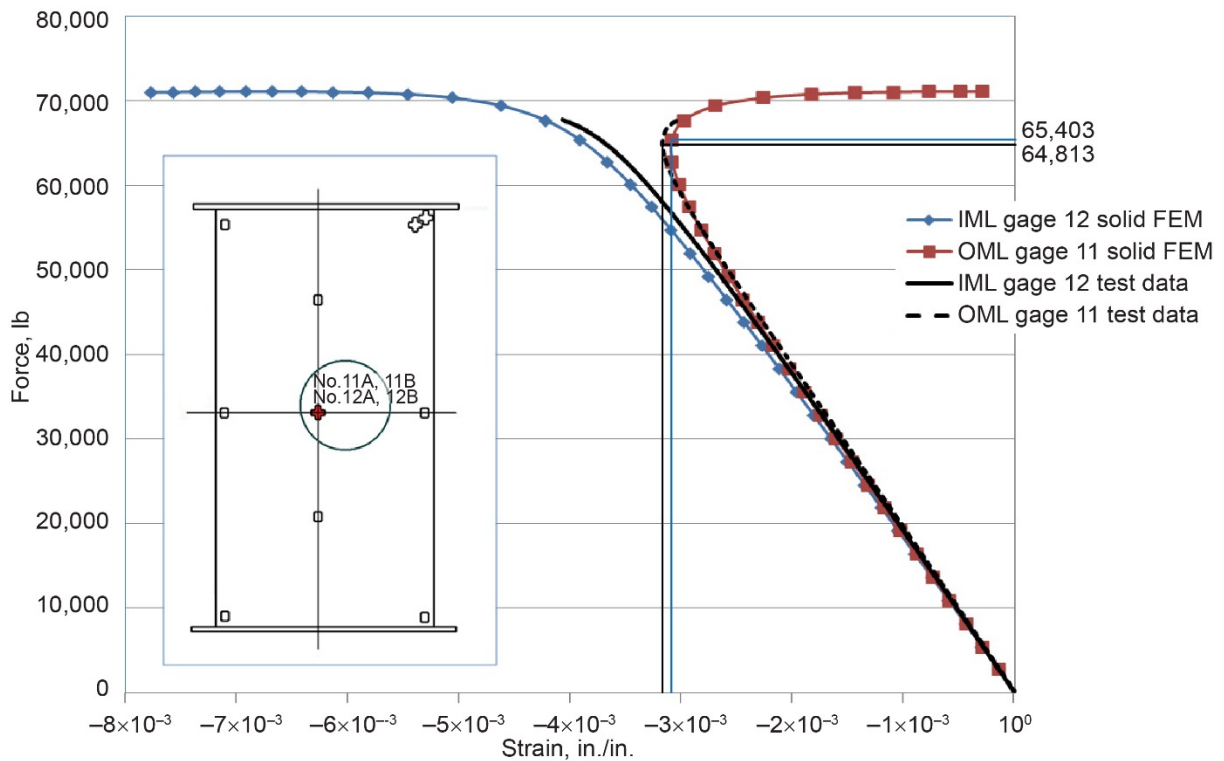

Figure 44.—Load versus minimum principal strain plot for gage numbers 11 and 12. Where FEM is finite element method, IML is inner mold line, and OML is outer mold line.
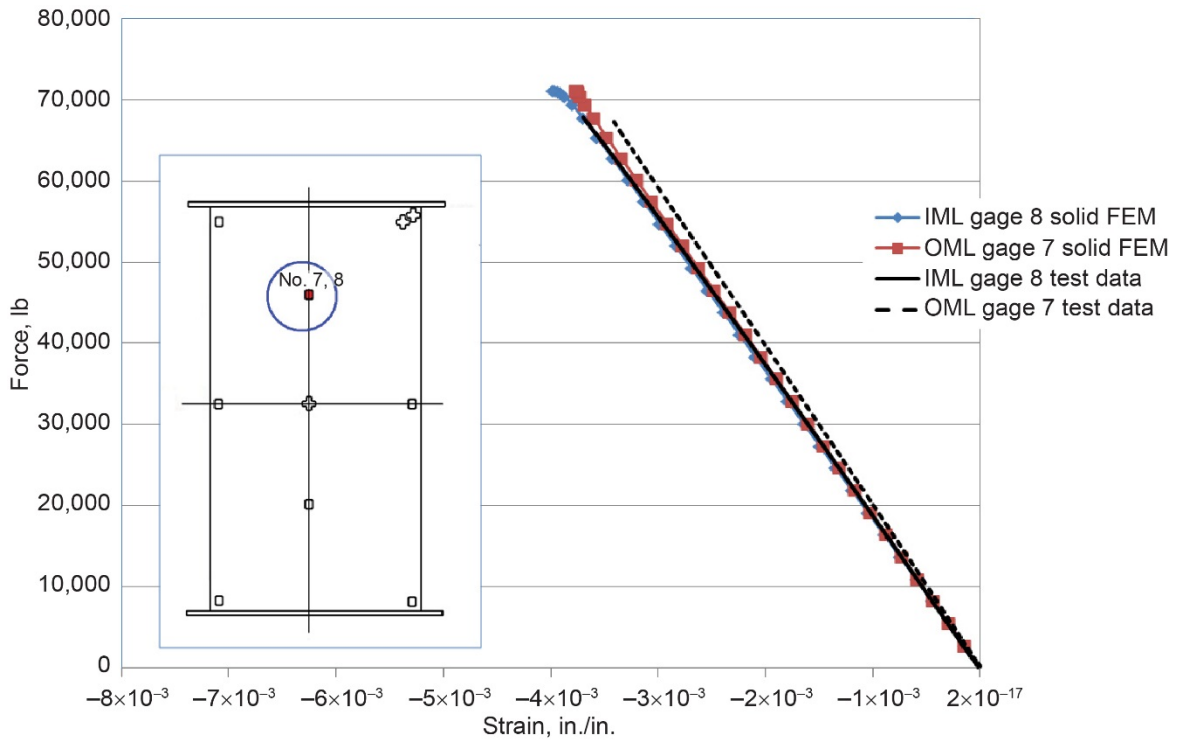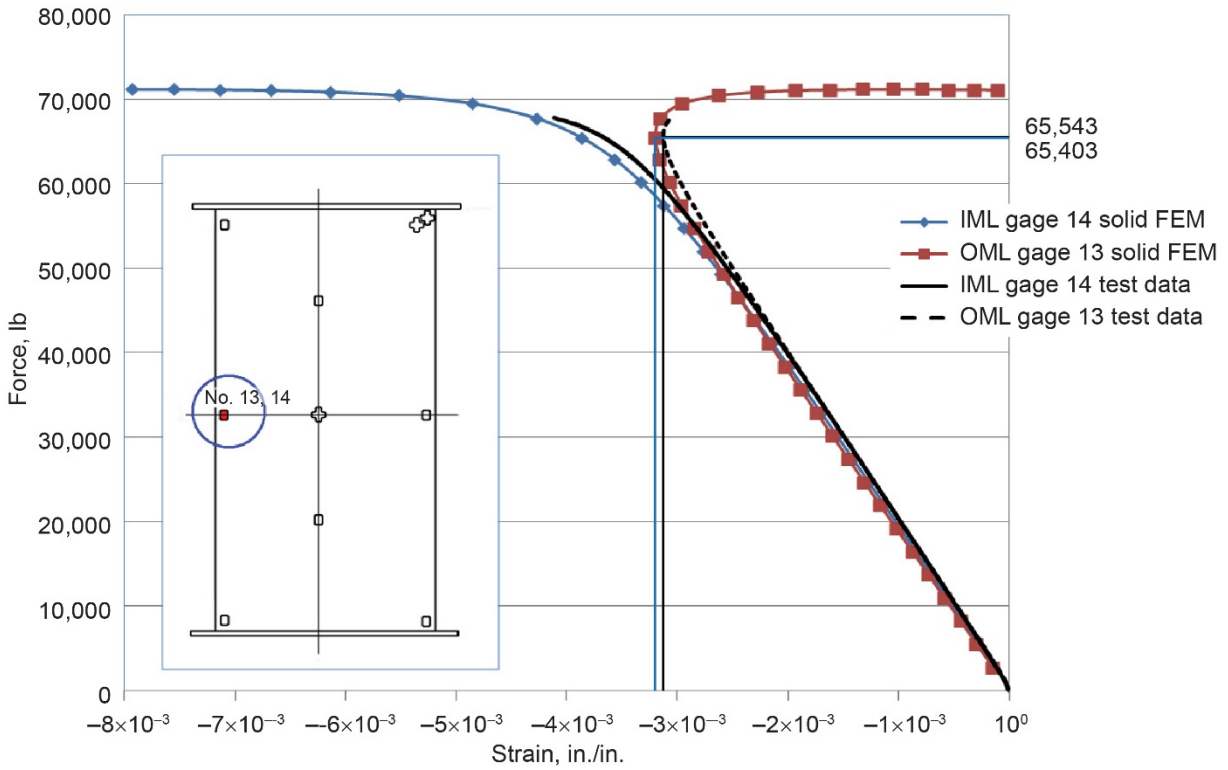
Figure 45.—Load versus minimum principal strain plot for gage numbers 13 and 14. Where FEM is finite element method, IML is inner mold line, and OML is outer mold line.

Figure 46.—Load versus minimum principal strain plot for gage numbers 15 and 16. Where FEM is finite element method, IML is inner mold line, and OML is outer mold line.

Figure 47.—Load versus minimum principal strain plot for gage numbers 17 and 18. Where FEM is finite element method, IML is inner mold line, and OML is outer mold line.
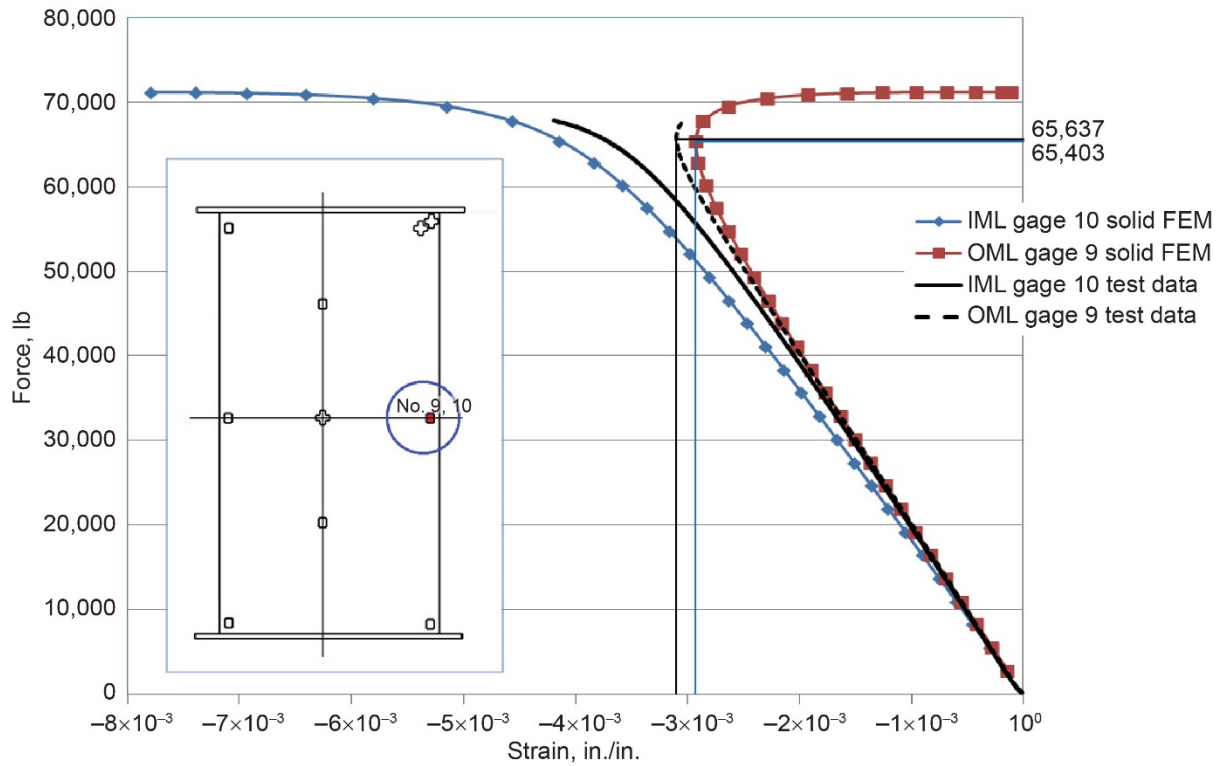

Figure 48.—Load versus minimum principal strain plot for gage numbers 19 and 20. Where FEM is finite element method, IML is inner mold line, and OML is outer mold line.
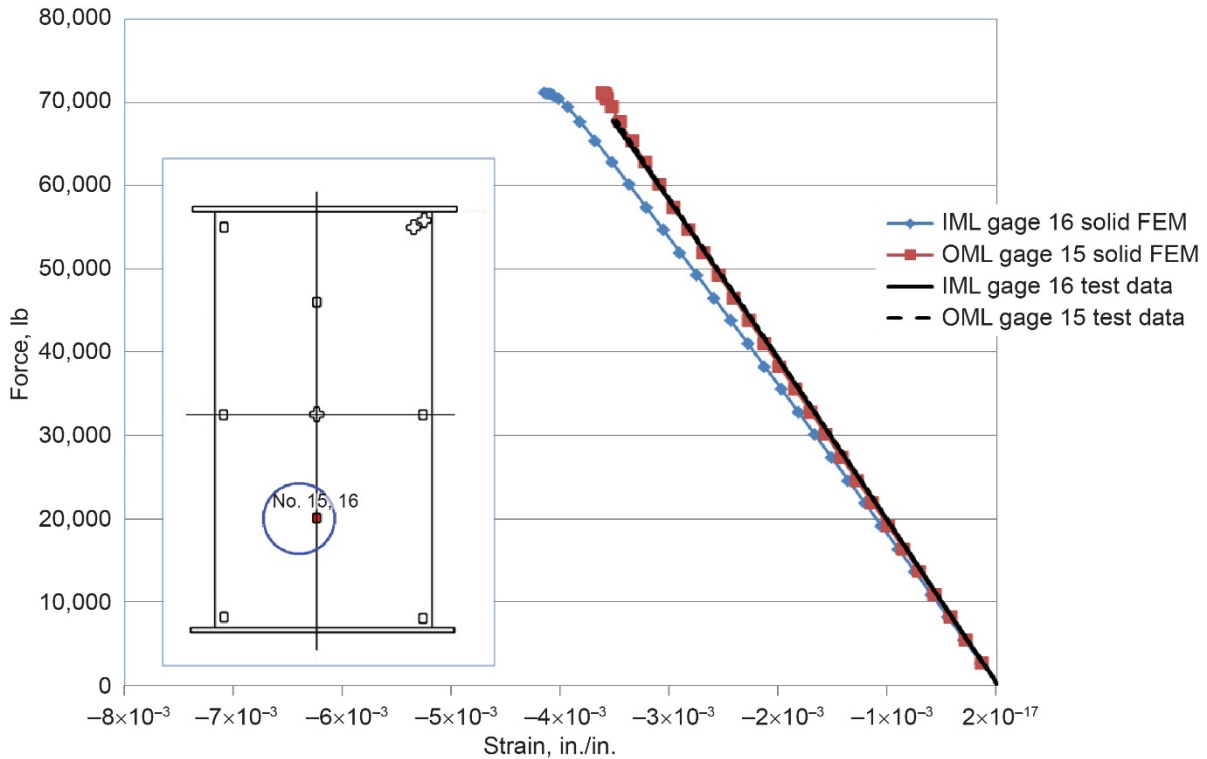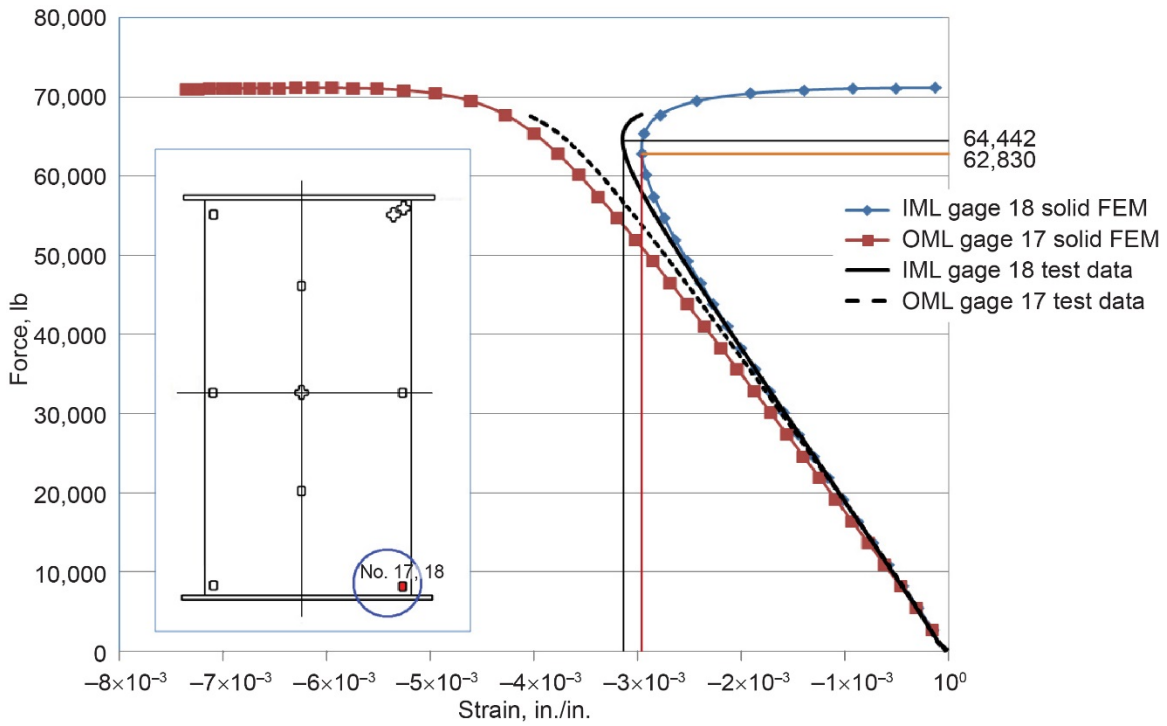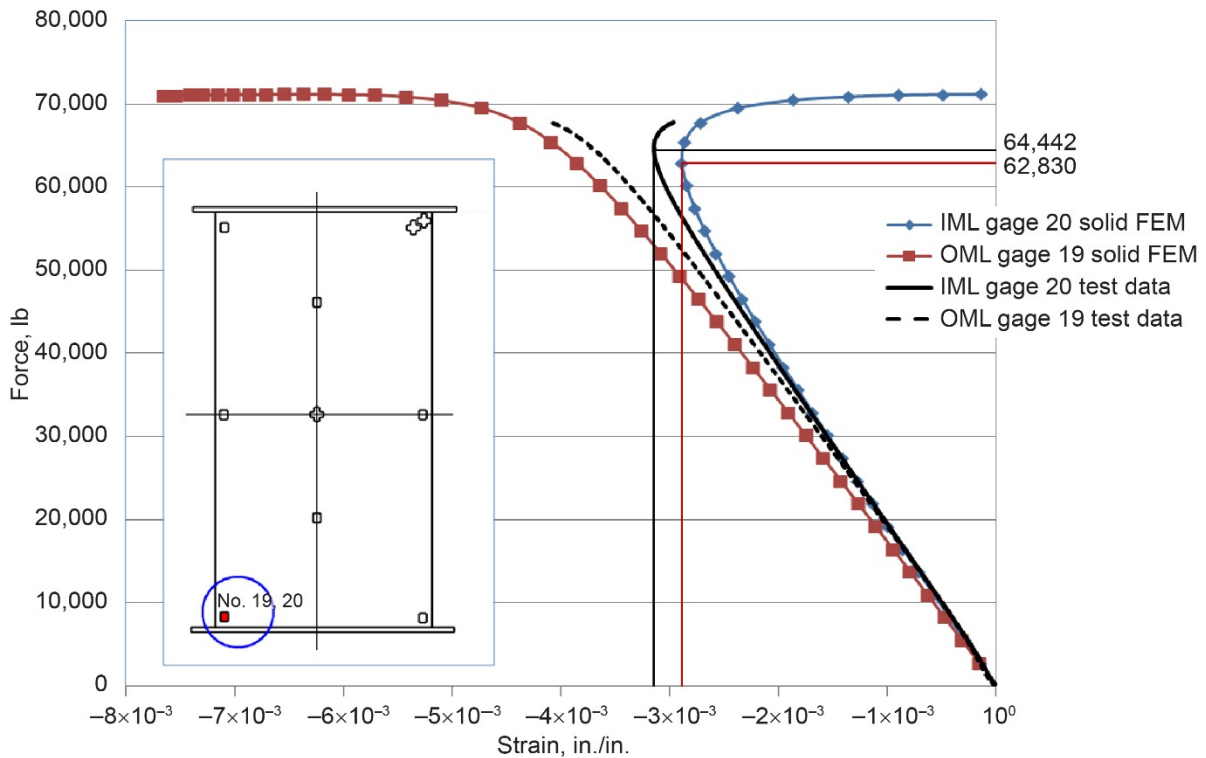
Figure 49 and Figure 50 show that the postbuckled, in-plane or longitudinal displacement photogrammetry results at 65,183, 66,950, and 68,178 lb qualitatively compared well with the analytical predictions at 65,403, 67,736, and 69,486 lb. In the ANSYS® solid element model, the nodal displacements vary slightly on the O.D. and I.D. surfaces. Figure 51 and Figure 52 show that the postbuckled, out-of-plane or radial displacements compare well qualitatively with the analytical predictions, on the I.D. and O.D. surfaces, respectively. However, the radial photogrammetry test results in Figure 51 and Figure 52 show symmetric contours about the vertical center of the panel. The analytical results show asymmetry in the radial displacements due to the asymmetry in the linear buckling mode shapes superimposed on the initial geometry. The out-of-plane displacements were the same for both the I.D. and O.D. surfaces.

For the I.D. surface, Figure 53 and Figure 54 show that the postbuckled, longitudinal (e_{xx}) strain test results at 65,183, 66,950, and 68,178 lb qualitatively compared well with the minimum principal strain analytical predictions at 65,403, 67,736, and 69,486 lb, respectively. The minimum principal strain (compressive) on the I.D. surface was not uniform through the progression of the applied loads as shown in Figure 53. The minimum principal strain (compressive) on the O.D. surface in Figure 54 was fairly uniform up until the load of 69,486 lb, which is past the buckling load of 65,403 lb predicted at gages 9, 11, and 13 listed in Table VII and shown in Figure 43, Figure 44, and Figure 45, respectively. The minimum principal strain was the primary strain in the buckling test.

The minimum principal strains on the I.D. surface in Figure 53 show the asymmetry in the ANSYS® solid FEM, which were a result of the scaled geometric imperfections superimposed from the linear buckling modes. The asymmetry in the minimum principal strains on the O.D. surface, shown in Figure 54, is less pronounced.

Figure 55 and Figure 56 show that the second principal strain also compared well with the in-plane lateral direction. The second principal strains in Figure 55 show the asymmetry on the I.D. surface in the ANSYS® solid FEM. Again, this was due to the scaled geometric imperfections superimposed from the linear buckling modes. The asymmetry is not as pronounced on the second principal strain plots for the O.D. surface. The photogrammetry lateral strains (e_{yy}) along the horizontal center of the test panel's I.D. are 30 percent greater than the second principal strain results from the FEM. The photogrammetry lateral strains along the horizontal center of the test panel's O.D. are 40 percent greater than the analytical second principal strain results. This may also be explained by the seeding of the linear buckling mode shapes onto the initial geometry. The actual panel imperfections drive the panel test strain results.

Figure 57 and Figure 58 show a comparison of the in-plane shear strains between the ANSYS® FEM results and the photogrammetry test results for the I.D. and O.D. surfaces, respectively. The shear strains from the analytical results at the corners of the panel I.D. are 33 to 67 percent greater than the tests results. The shear strains from the analytical results at the corners of the panel O.D. are 75 to 100 percent greater than the corresponding tests results. This implies that the FEM is much more constrained than the actual test panels.

Figure 49.—Postbuckling inner mold line axial (in-plane longitudinal) displacement comparison. (a) Analytical prediction of I.D. surface: 65,403 lb. (b) Photogrammetric results of I.D. surface: 65,183 lb. (c) Analytical prediction of I.D. surface: 67,736 lb. (d) Photogrammetric results of I.D. surface: 66,950 lb. (e) Analytical prediction of I.D. surface: 69,486 lb. (f) Photogrammetric results of I.D. surface: 68,178 lb. Where u(in) is axial displacement in x- and z-directions from experiment and UZ is axial displacement in x- and z-directions from ANSYS®.

Figure 50.—Postbuckling outer mold line (OML) axial (in-plane longitudinal) displacement comparison. (a) Analytical prediction of OML surface: 65,403 lb. (b) Photogrammetric results of OML surface: 65,183 lb. (c) Analytical prediction of OML surface: 67,736 lb. (d) Photogrammetric results of OML surface: 66,950 lb. (e) Analytical prediction of OML surface: 69,486 lb. (f) Photogrammetric results of OML surface: 68,178 lb. Where u(in) is axial displacement in z- and x-directions from experiment and UZ is axial displacement in x- and z-directions from ANSYS®.
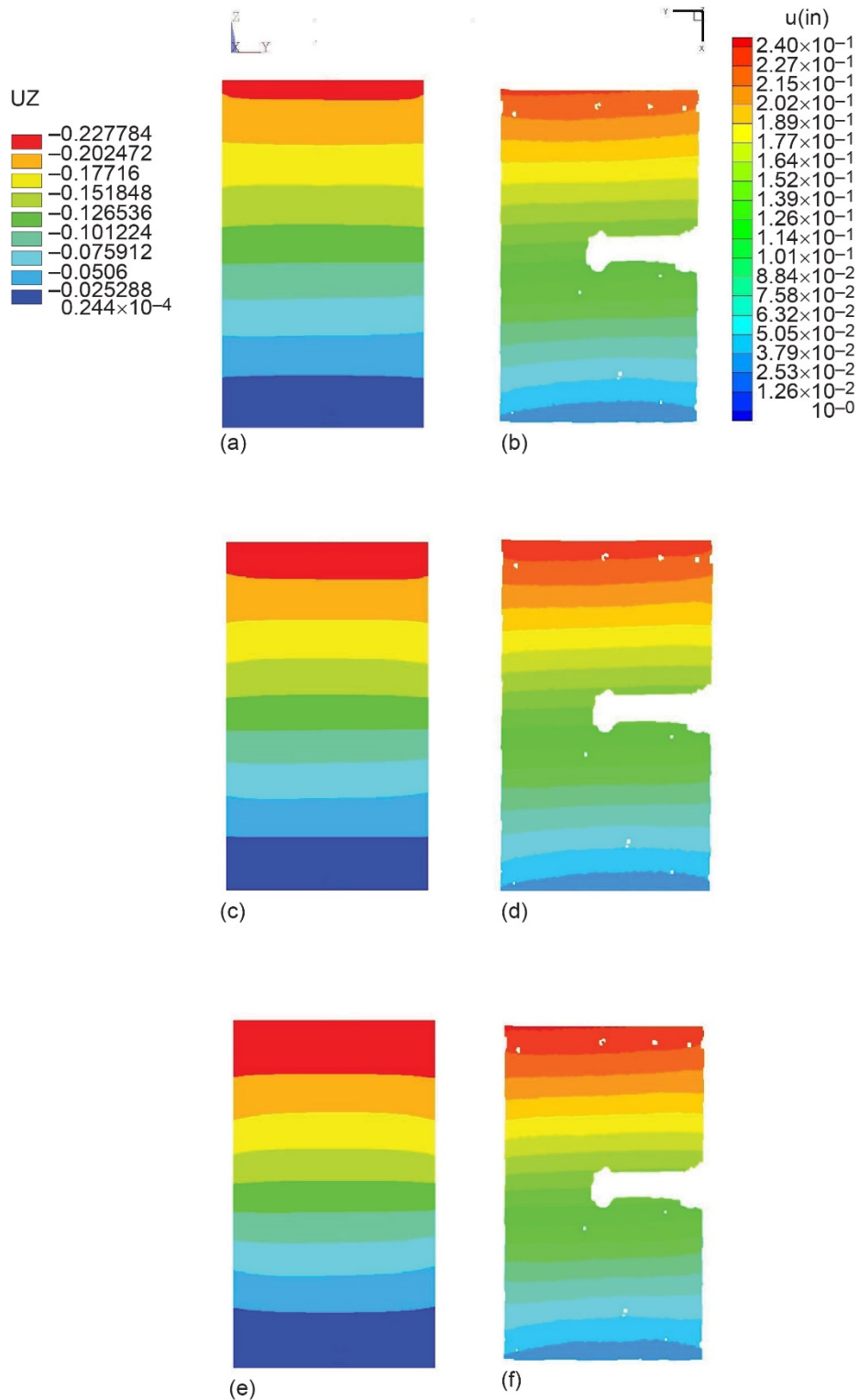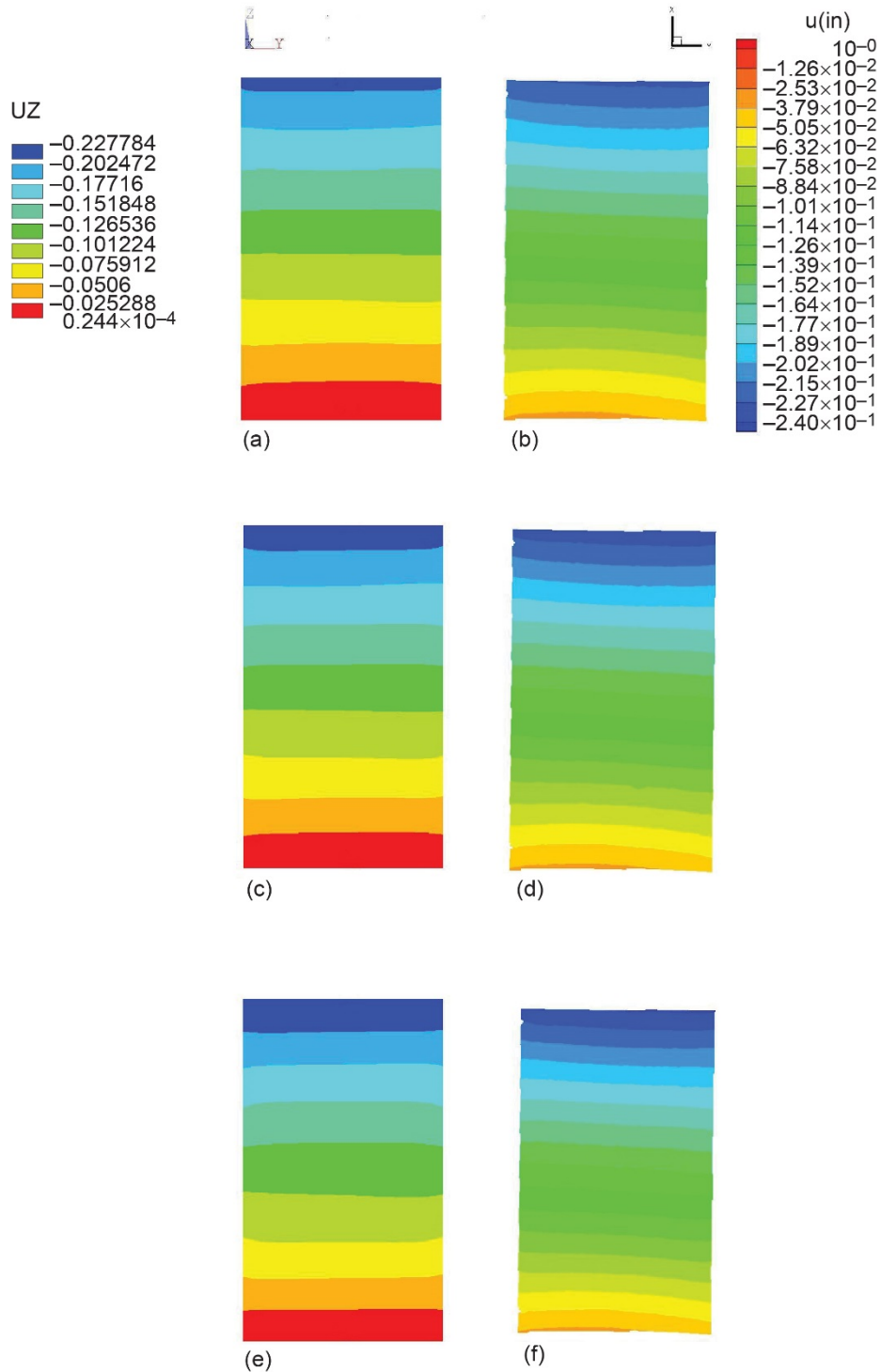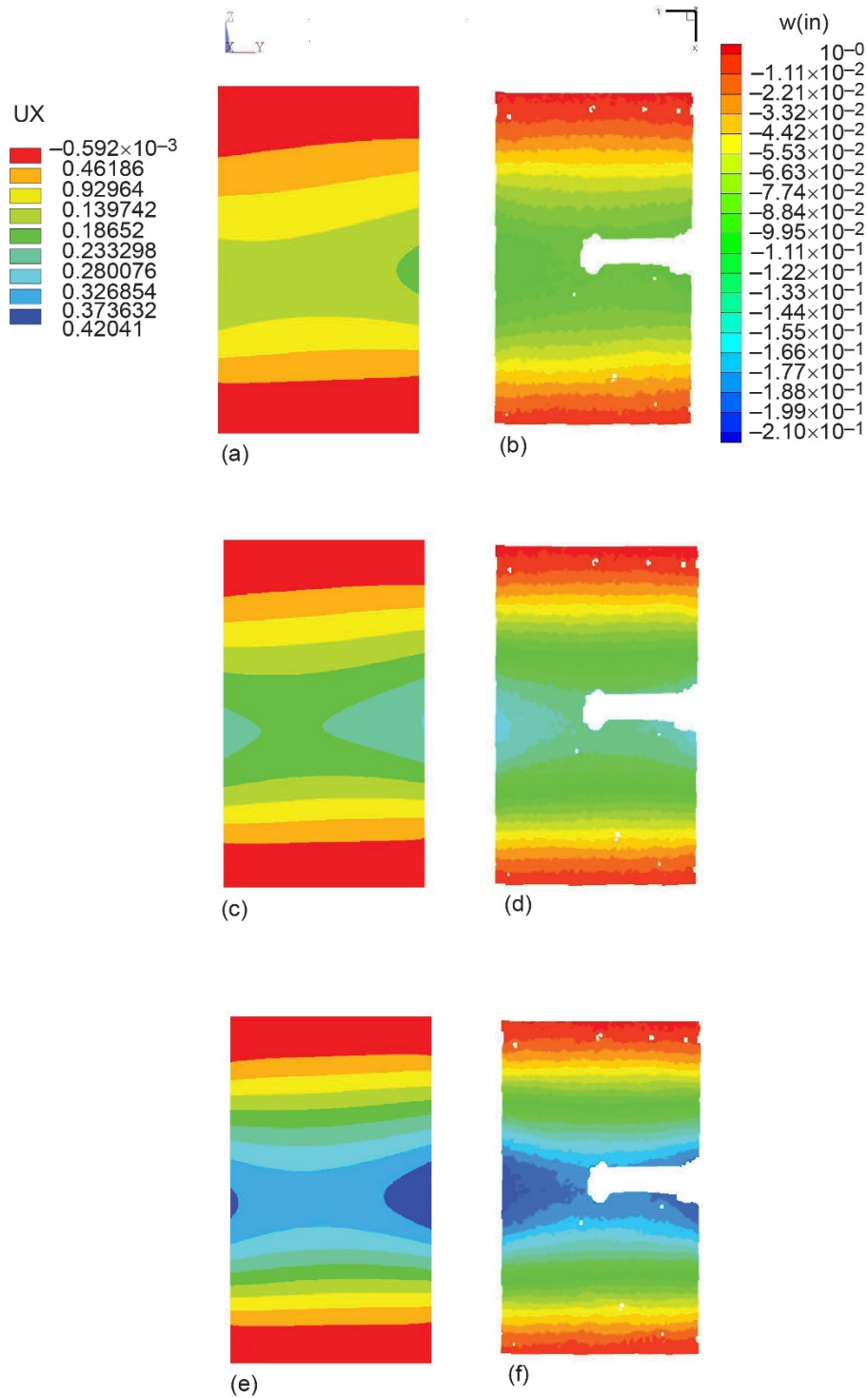
Figure 51.—Postbuckling inner mold line out-of-plane (radial) displacement comparison. (a) Analytical prediction of I.D. surface: 65,403 lb. (b) Photogrammetric results of I.D. surface: 65,183 lb. (c) Analytical prediction of I.D. surface: 67,736 lb. (d) Photogrammetric results of I.D. surface: 66,950 lb. (e) Analytical prediction of I.D. surface: 69,486 lb. (f) Photogrammetric results of I.D. surface: 68,178 lb. Where UX is out-of-plane displacement in x- and z- directions from ANSYS® and w(in) is out-of-plane displacement in x- and z-directions from experiment.
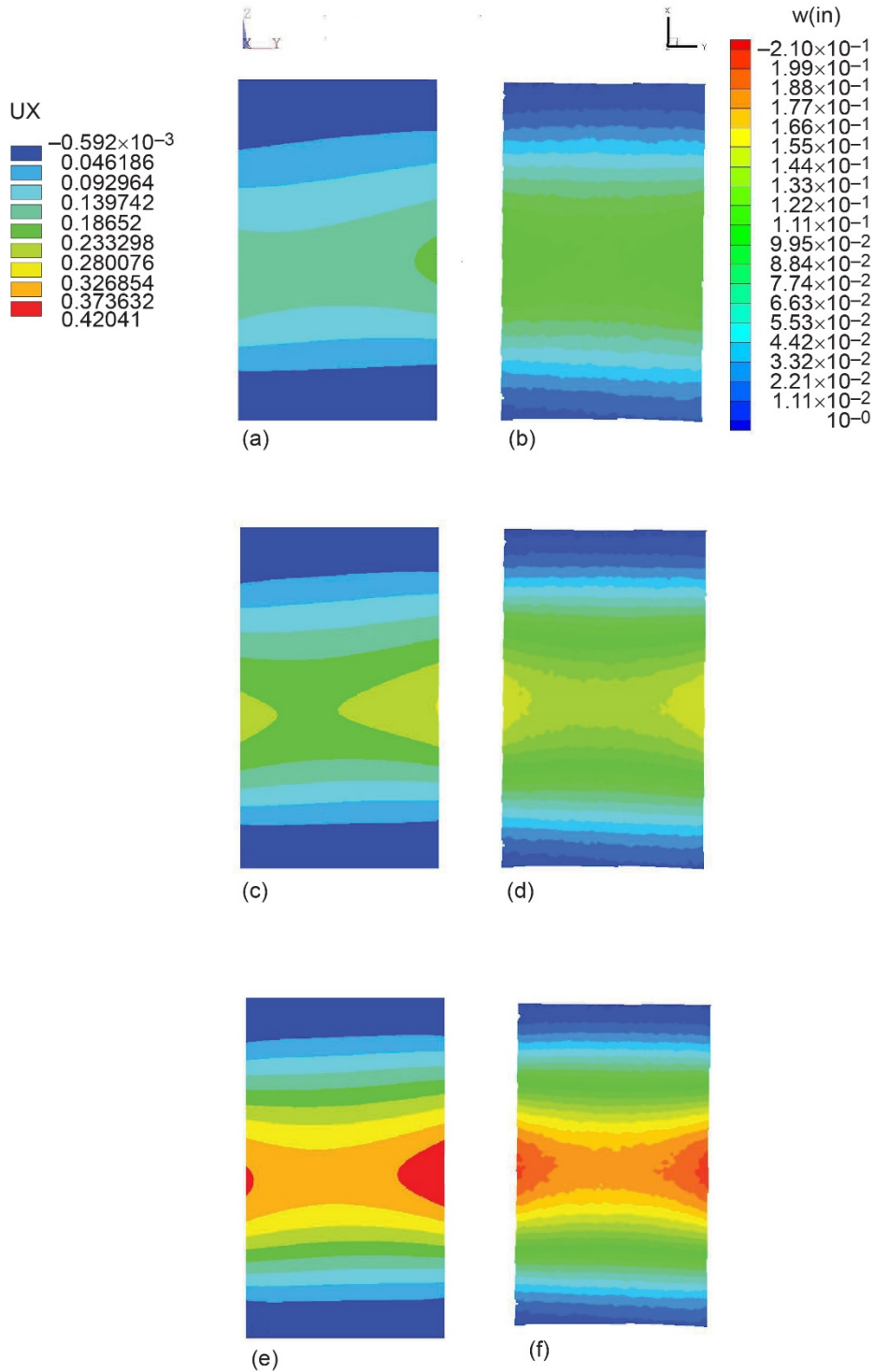
Figure 52.—Postbuckling outer mold line out-of-plane (radial) displacement comparison.
(a) Analytical prediction of OML surface: 65,403 lb. (b) Photogrammetric results of OML
surface: 65,183 lb. (c) Analytical prediction of OML surface: 67,736 lb. (d) Photogrammetric
results of OML surface: 66,950 lb. (e) Analytical prediction of OML surface: 69,486 lb.
(f) Photogrammetric results of OML surface: 68,178 lb. Where UX is out-of-plane
displacement in x- and z- directions from ANSYS® and w(in) is out-of-plane displacement in
x- and z-directions from experiment.
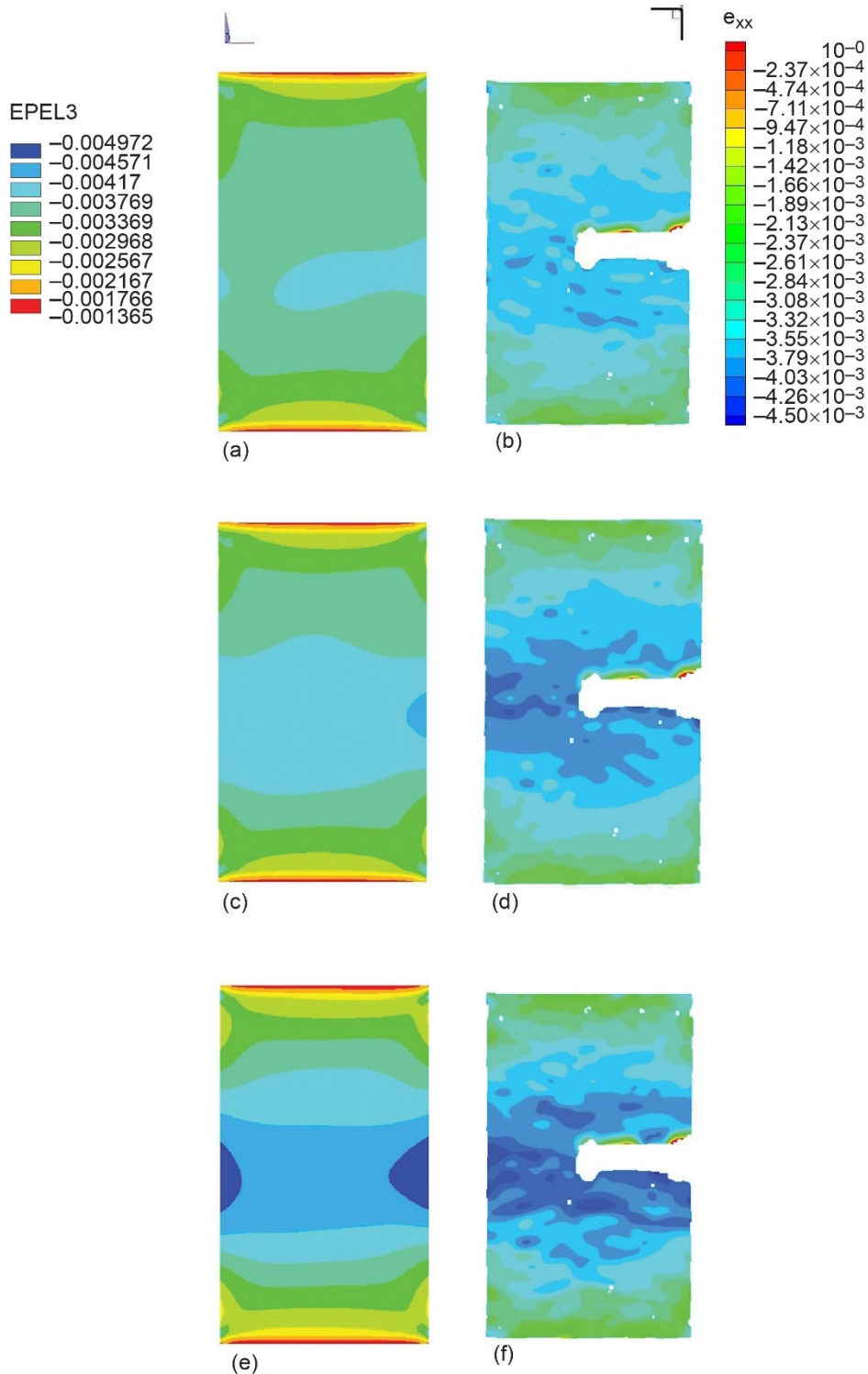
Figure 53.—Postbuckling inner mold line minimum principal (longitudinal) strain comparison. (a) Analytical prediction of I.D. surface: 65,403 lb. (b) Photogrammetric results of I.D. surface: 65,183 lb. (c) Analytical prediction of I.D. surface: 67,736 lb. (d) Photogrammetric results of I.D. surface: 66,950 lb. (e) Analytical prediction of I.D. surface: 69,486 lb. (f) Photogrammetric results of I.D. surface: 68,178 lb. Where e_{xx} is minimum principal strain from experiment and EPEL3 is minimum principal strain from ANSYS®.

Figure 54.—Postbuckling outer mold line (OML) minimum principal (longitudinal) strain comparison. (a) Analytical prediction of OML surface: 65,403 lb. (b) Photogrammetric results of OML surface: 65,183 lb. (c) Analytical prediction of OML surface: 67,736 lb. (d) Photogrammetric results of OML surface: 66,950 lb. (e) Analytical prediction of OML surface: 69,486 lb. (f) Photogrammetric results of OML surface: 68,178 lb. Where e_{xx} is minimum principal strain from experiment and EPEL3 is minimum principal strain from ANSYS®.

Figure 55.—Postbuckling inner mold line second principal (circumferential or hoop) strain comparison. (a) Analytical prediction of I.D. surface: 65,403 lb. (b) Photogrammetric results of I.D. surface: 65,183 lb. (c) Analytical prediction of I.D. surface: 67,736 lb. (d) Photogrammetric results of I.D. surface: 66,950 lb. (e) Analytical prediction of I.D. surface: 69,486 lb. (f) Photogrammetric results of I.D. surface: 68,178 lb. Where e_{yy} is second principal strain from experiment and EPEL2 is second principal strain from ANSYS®.
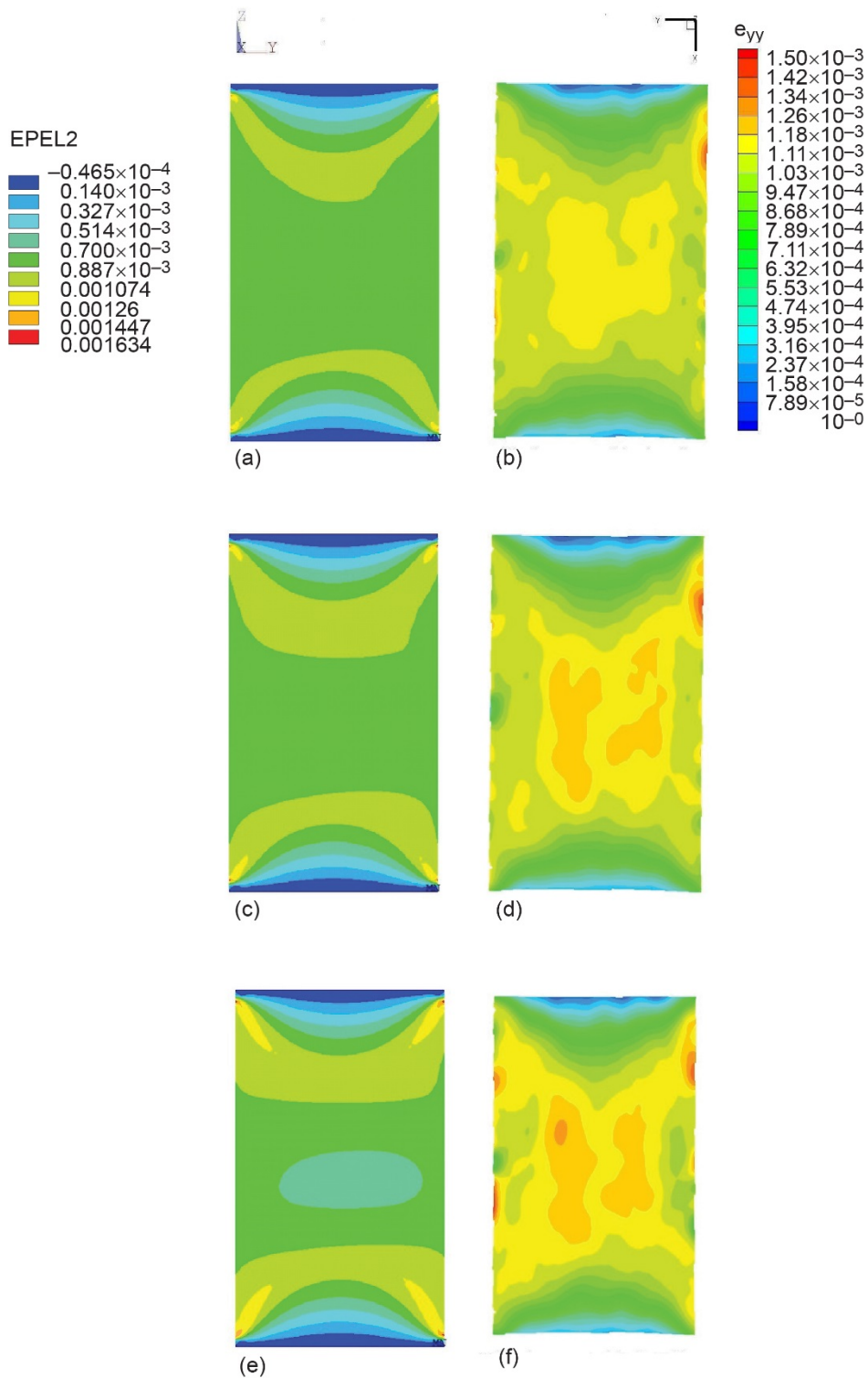
Figure 56.—Postbuckling outer mold line (OML) second principal (circumferential or hoop) strain comparison. (a) Analytical prediction of OML surface: 65,403 lb. (b) Photogrammetric results of OML surface: 65,183 lb. (c) Analytical prediction of OML surface: 67,736 lb. (d) Photogrammetric results of OML surface: 66,950 lb. (e) Analytical prediction of OML surface: 69,486 lb. (f) Photogrammetric results of OML surface: 68,178 lb. Where e_{yy} is second principal strain from experiment and EPEL2 is second principal strain from ANSYS®.
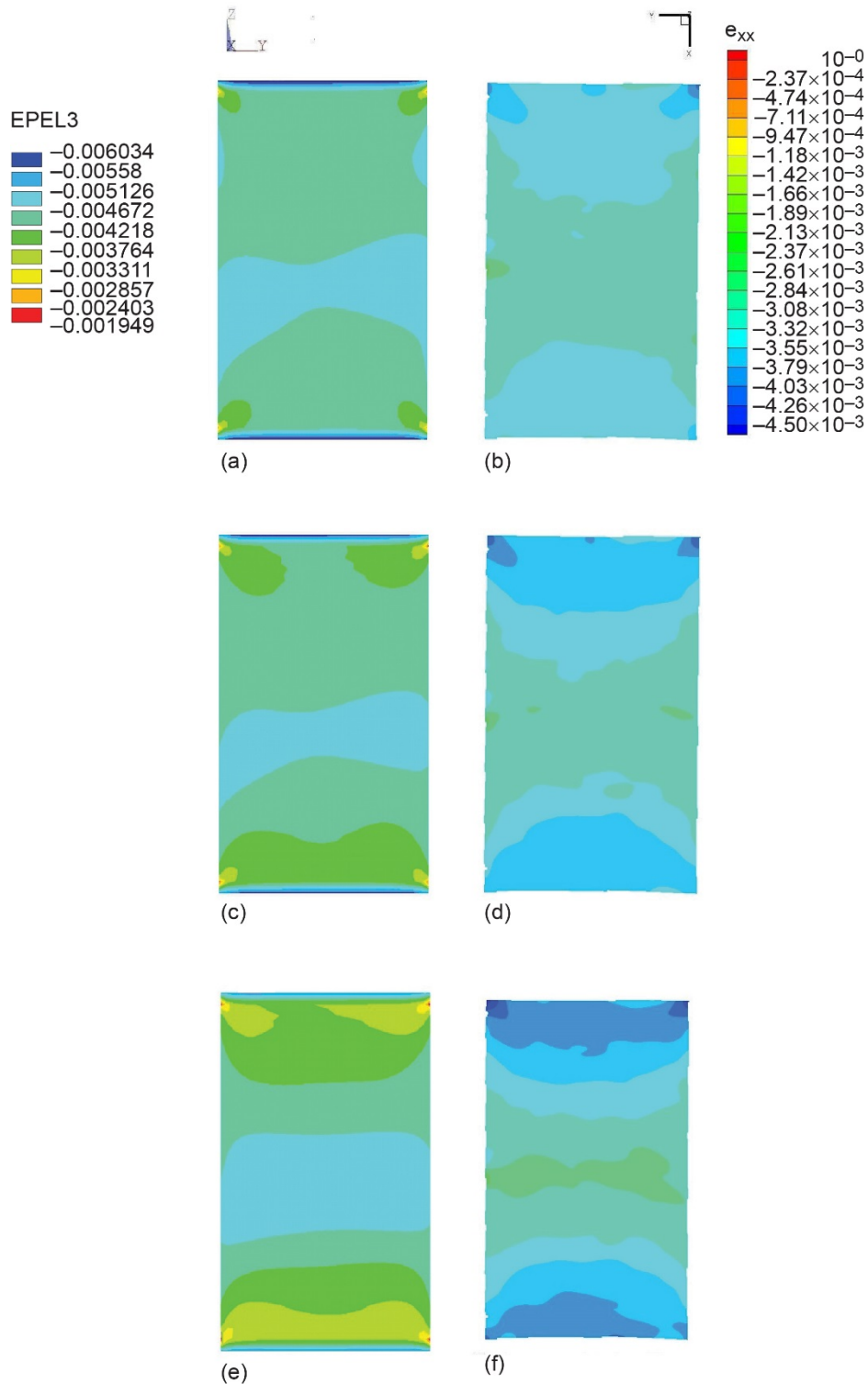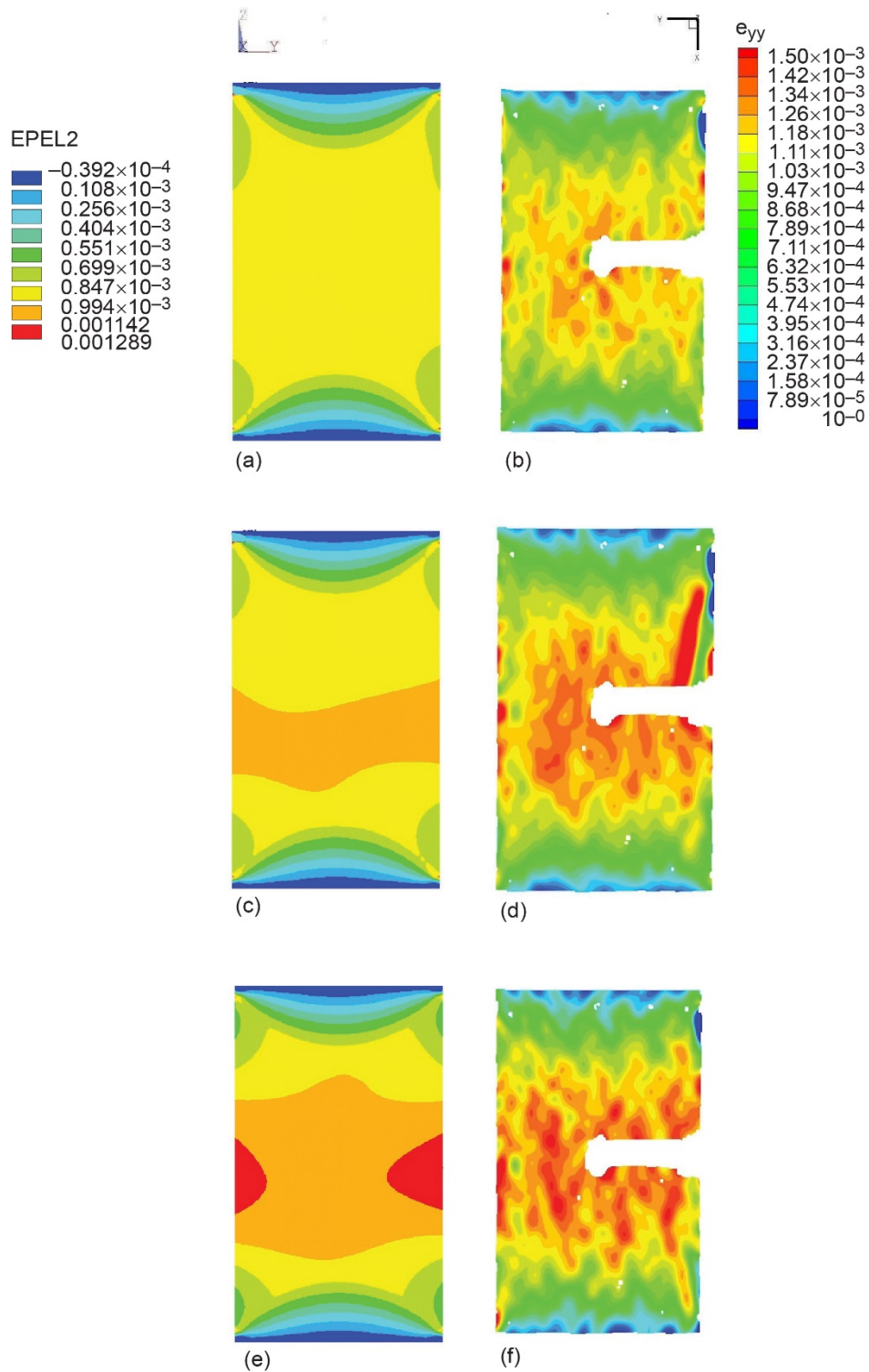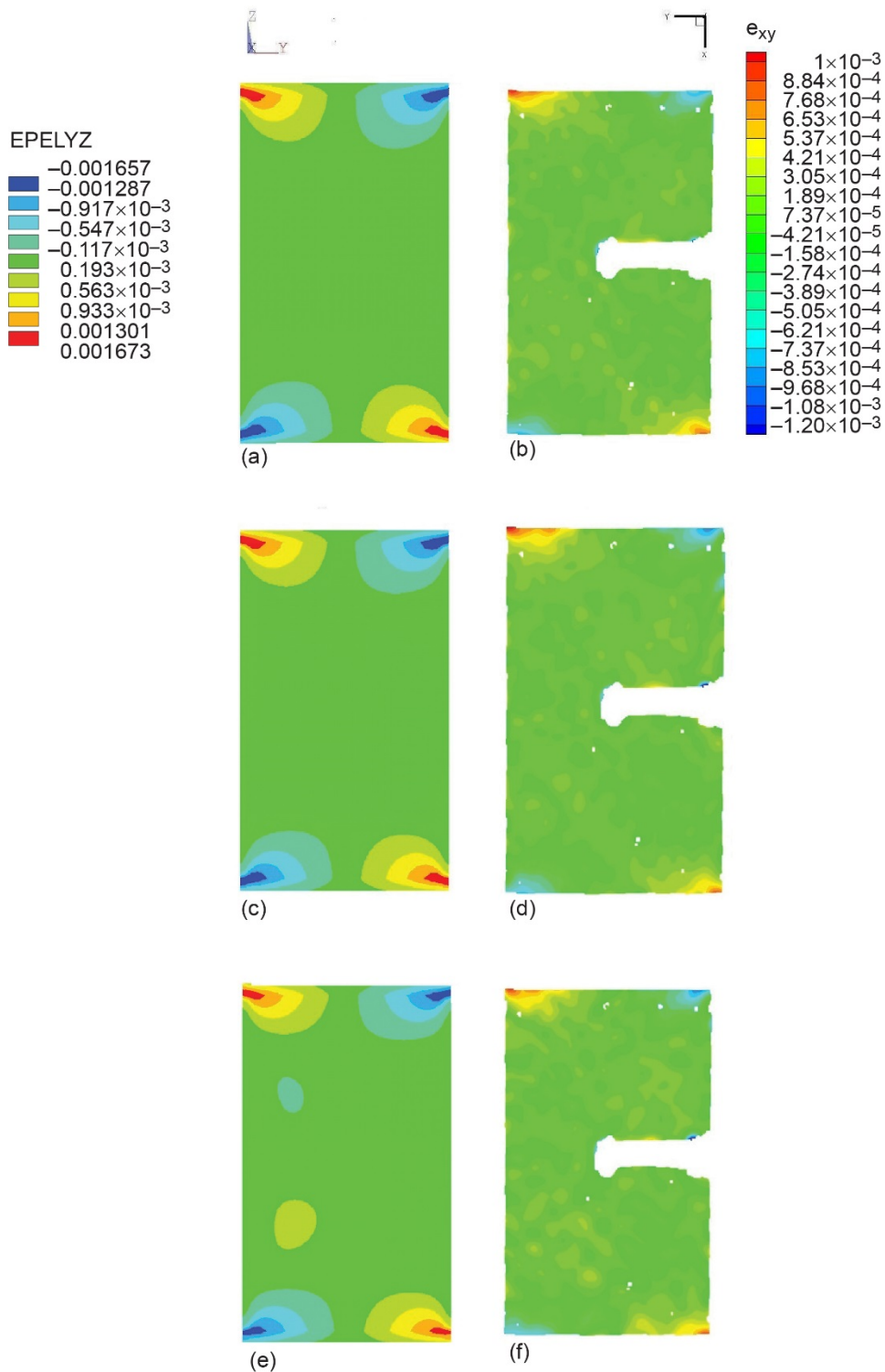
Figure 57.—Postbuckling inner mold line in-plane shear strain comparison. (a) Analytical prediction of I.D. surface: 65,403 lb. (b) Photogrammetric results of I.D. surface: 65,183 lb. (c) Analytical prediction of I.D. surface: 67,736 lb. (d) Photogrammetric results of I.D. surface: 66,950 lb. (e) Analytical prediction of I.D. surface: 69,486 lb. (f) Photogrammetric results of I.D. surface: 68,178 lb. Where e_{xy} is in-plane shear strain from experiment and EPEYZ is in-plane shear strain from ANSYS®.

Figure 58.—Postbuckling outer mold line (OML) in-plane shear strain comparison.
(a) Analytical prediction of OML surface: 65,403 lb. (b) Photogrammetric results of
OML surface: 65,183 lb. (c) Analytical prediction of OML surface: 67,736 lb.
(d) Photogrammetric results of OML surface: 66,950 lb. (e) Analytical prediction of
OML surface: 69,486 lb. (f) Photogrammetric results of OML surface: 68,178 lb. Where
e_{xy} is in-plane shear strain from experiment and EPEYZ is in-plane shear strain from
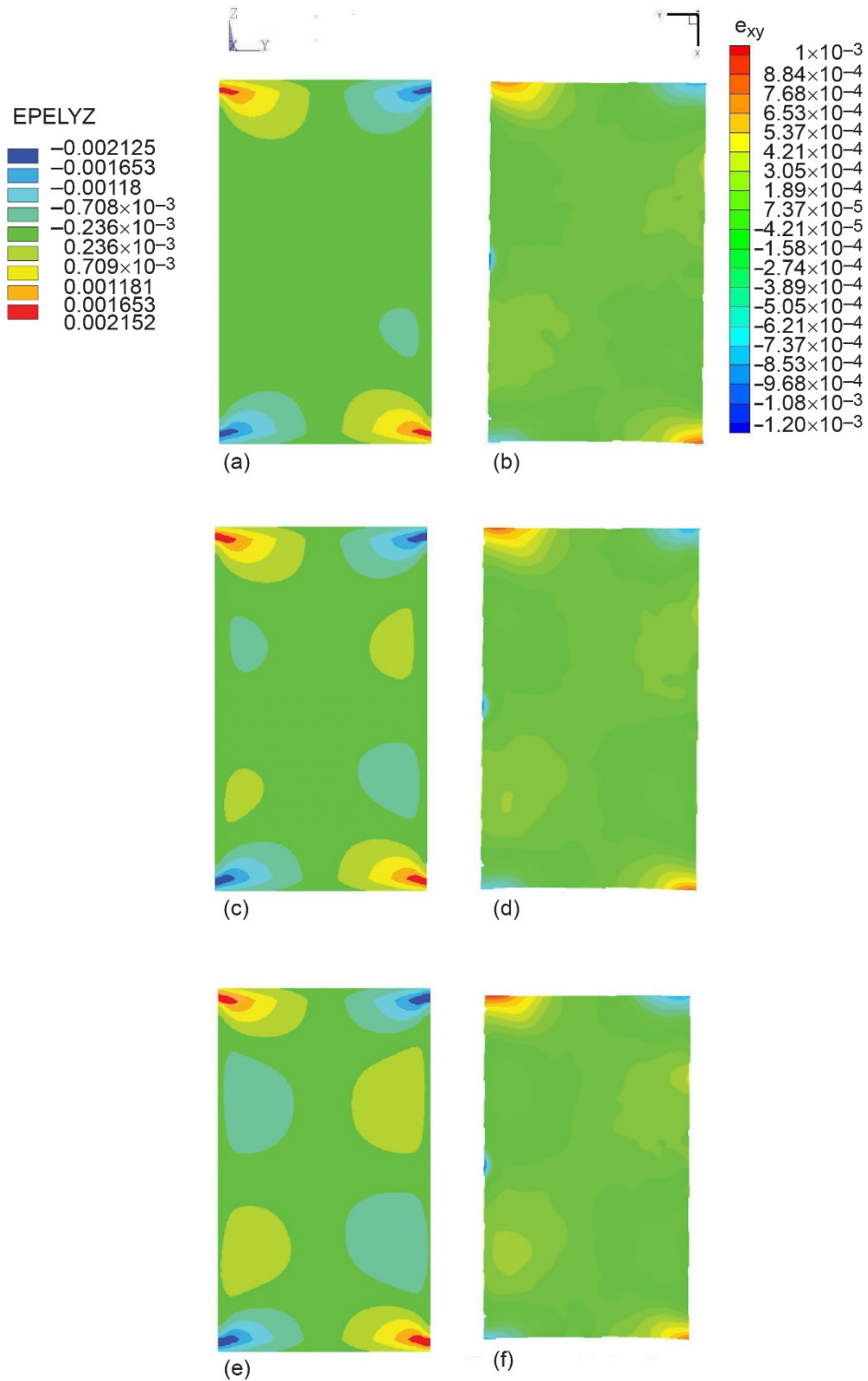ANSYS®.

5.0   Conclusions

Experimental and analytical results have been presented pertaining to the buckling of a 3- by 5-ft-curved sandwich panel: Panel D. The panel was composed of a 1.125 in.-thick aluminum honeycomb core and six-ply, quasi-isotropic, OOA cured, T40-800B/5320-1, laminated composite facesheets cut from a $1/16^{th}$ arc segment of a 10-m barrel. Experimental and modeling success was evaluated using specifically defined criteria. Additionally, various parametric studies were performed to determine the impact of manufacturing defects and modeling techniques.

The experimental success criteria were described, all of which were met. Namely, all critical instrumentation was fully operational during the test, loads were applied as described in this document, and the maximum attained load and all associated data were recorded and saved. The panel exhibits catastrophic strength failure prior to buckling, although no pre-existing damage was determined with nondestructive evaluation (NDE). However, failure of the panel did not negatively affect the success criteria metrics.

Additionally, the modeling success criteria were also achieved: the buckling load was predicted within 20 percent (despite the premature failure observed in the experiment), the buckling mode and direction were predicted correctly, and the local strain fields correlated well with visual imaging data measured during the experiment.

Both linear eigenvalue and geometrically nonlinear analyses were performed by using a variety of commercially available finite element method (FEM) software tools to predict the buckling load of the honeycomb sandwich panel. The linear eigenvalue prediction fell within ~19 percent above the experimental buckling load. Surface imperfection measurements were introduced into the FEM model through a swept bow, and geometrically nonlinear analyses were utilized to predict the buckling load via progressive collapse simulations. The simulations yielded a buckling load prediction within ~19 percent higher than the experimental load. Furthermore, the direction of buckling (toward the O.D.) was predicted correctly, which was a direct consequence of including the measured geometric imperfections in the model. Full-field displacement and strain measurements predicted with the nonlinear analysis also corresponded well qualitatively with experimental visual image correlation (VIC) data. Finally, linear strength analyses were completed at the buckling load, and they ensured that the predicted panel failure was driven by stiffness (i.e., buckling), not strength, as was observed in test.

Shell-based nonlinear buckling analyses of various honeycomb sandwich panel sizes showed that, once again, the buckling predictions of ANSYS® and Abaqus were in very good agreement. In ANSYS®, the first ten linear eigenvalues were used to seed the nonlinear analyses with geometric imperfections. Then, a detailed nonlinear buckling analysis study was performed with an ANSYS® solid element model of the Panel D 3- by 5-ft arc segment sandwich panel. First, this model was used to show good agreement with the ANSYS® shell element based nonlinear model in terms of mode and buckling load. Then, detailed strain histories were examined at various strain gage locations on the test panel. By monitoring the strain histories on the front and back sides of the panel at a given location, it was shown that the point of a strain reversal could be used as an estimate of the onset of buckling. In the solid FEM, analytical predictions of the postbuckled, in-plane or longitudinal displacements compared well with the photogrammetry test results. The analytical predictions of the postbuckled, out-of-plane or radial, displacement load compared well qualitatively with the test results. However, contour plots of the analytical out-of-plane or radial displacements do not compare well with the photogrammetry test results. This is primarily due to the seeding of the first ten linear eigenvalues in the nonlinear analyses to produce geometric imperfections. The actual panel imperfections likely drive the shape of the panel's out-of-plane

displacements seen in the photogrammetry results. Whereas the contour shapes from the ANSYS® solid FEM are a function of the first ten eigenvalues that were superimposed on the initial panel geometry.

No conclusions could be drawn about the cause of the strength failure of the experimental panel. As a result of this failure, the 2-D analytical predictions (which did not include failure modeling) exhibited significant error when compared to test data, however the predictions were improved with the 3D modeling. Previous work has shown that the analysis methods presented in this paper are valid for predicting the buckling load of large honeycomb structures when there is no onset of failure. Measured geometric imperfections were included in the FEM models to yield more accurate predictions of the buckling load of undamaged panels. Although the results of this study cannot be directly applied to obtain better estimates of the buckling loads (beyond eigenvalue analysis) of full cylinders or larger cylinder segments (as the buckling modes and imperfection sensitivities are different for these different geometries), the practices presented here can be used to determine the same sensitivities of these other structures to similar geometric imperfections. In the future, such studies may lead to more comprehensive linear bucking knockdown factors for cylindrical shells that consider the impact and degree of different imperfections or defects separately. Furthermore, sensitivity studies can be utilized to arrive at critical manufacturing tolerances.

Appendix—Nomenclature

APDL	ANSYS® Parametric Design Language
CMDP	composite manufacturing demonstration panel
CoEx	Composites for Exploration
DCDT	direct-current displacement transducer
FEA	finite element analysis
FEM	finite element method
HLLV	Heavy Lift Launch Vehicle
I.D.	inner diameter
IA	in-autoclave
IML	inner mold line
IR	infrared
MSC	MacNeal-Schwendler Corporation
MTP	manufacturing test panel
Nastran	NASA STRucture ANalysis
NDE	nondestructive evaluation
O.D.	outer diameter
OML	outer mold line
OOA	out-of-autoclave
VIC	visual image correlation

Symbols

e_{xx}	minimum principal strain from experiment
e_{xy}	in-plane shear strain from experiment
e_{yy}	second principal strain from experiment
E	Young's modulus of V-100 potting compound
E_1	longitudinal moduli
E_2	transverse moduli
E_3	honeycomb normal (out-of-plane) modulus
EPEL2	second principal strain from ANSYS®
EPEL3	minimum principal strain from ANSYS®
EPELYZ	in-plane shear strain from ANSYS®
F_{c1}	compressive strength of core used in analyses
F_{c2}	compressive strength of core used in analyses
F_{c3}	compressive strength of core used in analyses
F_{s12}	shear strength of core used in analyses
F_{s13}	shear strength of core used in analyses
F_{s23}	shear strength of core used in analyses
F_{t1}	tensile strength of core used in analyses
F_{t2}	tensile strength of core used in analyses
F_{t3}	tensile strength of core used in analyses
G_{12}	in-plane shear modulus
G_{13}	shear modulus of core in ANSYS model
G_{23}	shear modulus of core in ANSYS model
G_{1Z}	shear modulus of core used in NASTRAN and Abaqus models

G_{2Z}	shear modulus of core used in NASTRAN and Abaqus models
I	node location
J	node location
K	node location
L	node location
M	node location
M11	out of plane moment
M12	out of plane moment
M21	out of plane moment
M22	out of plane moment
MN	location of minimum value
MX	location of maximum value
N	node location
N11	node N 11 location
N12	node N 12 location
N22	node N 22 location
O	node location
P	node location
P_{cr}	critical buckling load
Q_{13}	transverse shear force
Q_{23}	transverse shear force
Sx	stress, SOLSH190
SX	stress SHELL281
Sy	stress, SOLSH190
SY	stress SHELL281
Sz	stress, SOLSH190
u(in)	axial displacement in x- and z-directions from experiment
U, U1	out-of-plane displacement in x-direction from analysis
UX	out-of-plane displacement in x- and z-directions from experiment
Ux	out-of-plane displacement in x-direction
UZ	axial displacement in x- and z-directions from ANSYS®
w(in)	out-of-plane displacement in x- and z-direction from experiment
x	ply x-axis in fiber or ply longitudinal direction (Figure 29)
x_0	element x-axis if element orientation is not provided
y	ply y-axis direction: in-plane transverse to fiber or ply direction (Figure 29)
y_0	element y-axis if element orientation is not provided
y_{IJ}	IJ side of y-axis
z	ply z-axis direction: normal to ply plane, interlaminar direction (Figure 29)
z_0	finite element z-axis (Figure 29)
ε_A	membrane strain
ρ	core density used in NASTRAN and Abaqus models
ν	Poisson's ratio of film adhesive
ν_{12}	Poisson's ratio (in-plane transverse due to longitudinal load)
ν_{13}	Poisson's ratio (out-of-plane due to longitudinal load)
ν_{23}	Poisson's ratio (out-of-plane due to transverse load)
θ	ply angle

γ   weight density in pounds per cubic inch used in ANSYS model (Table VI)

μ   weight density in pounds per cubic foot (Table VI)

Subscript

s   indicates layup is symmetric about neutral plane of facesheet

References

ANSYS: DesignModeler User Guide. Release 14.0, SAS IP, Inc., Canonsburg, PA, 2011.

Hause, Terry; Johnson, Theodore F.; and Librescu, Livin: Effect of Face-Sheet Anisotropy on Buckling and Postbuckling of Sandwich Plates. J. Spacecr. Rockets, vol. 37, no. 3, 2000, pp. 331–341.

Hause, Terry; Librescu, Liviu; and Johnson, Thedore F.: Non-Linear Response of Geometrically Imperfect Sandwich Curved Panels Under Thermomechanical Loading. Int. J. Nonlinear Mech., vol. 33, no. 6, 1998, pp. 1039–1059.

Haynie, Waddy T., et al.: Validation of Lower-Bound Estimates for Compression-Loaded Cylindrical Shells. AIAA 2012–1689, 2012.

Hilburger, Mark W.: Developing the Next Generation Shell Buckling Design Factors and Technologies. AIAA 2012–1686, 2012.

Hilburger, Mark W.; Nemeth, Michael P.; and Starnes, James H., Jr.: Nonlinear and Buckling Behavior of Curved Panels Subjected to Combined Loads. AIAA 2001–1398, 2001.

Hilburger, Mark W.; and Starnes, James H., Jr.: Effects of Imperfections on the Buckling Response of Compression-Loaded Composite Shells. Int. J. Nonlinear Mech., vol. 37, nos. 4–5, 2002, pp. 623–643.

Hong, C.S.; and Jun S.M.: Buckling Behavior of Laminated Composite Cylindrical Panel With Initial Imperfections. Proceedings of the Symposium, ASME Winter Annual Meeting, San Francisco, CA, 1989, p. 9–15.

HyperSizer Structural Sizing Software. Collier Research Corp., Newport News, VA, 2012. www.HyperSizer.com Accessed June 25, 2018.

Jones, Robert M.: Mechanics of Composite Materials. Second ed., Taylor & Francis, Inc., Philadelphia, PA, 1999.

Kellas, Sotiris; Lerch, Brad; and Wilmoth, Nathan: Mechanical Characterization of In- and Out-of-Autoclave Cured Composite Panels for Large Launch Vehicles. Paper presented at SAMPE 2012, Baltimore, MD, 2012.

Kriegesmann, B.; Hilburger, Mark W.; and Rolfes, Raimund: The Effects of Geometric and Loading Imperfections on the Response and Lower-Bound Buckling Load of a Compression-Loaded Cylindrical Shell. AIAA 2012–1864, 2012.

Lockheed Martin: Orion Materials and Design Allowables. Rev. D, Sept. 22, 2010.

Ley, Robert P.; Lin, Weichuan; and Mbanefo, Uy: Facesheet Wrinkling in Sandwich Structures. NASA/CR—1999-208994, 1999. http://ntrs.nasa.gov

Lynch, C., et al.: The Computational Post Buckling Analysis of Fuselage Stiffened Panels Loaded in Compression. Thin Wall. Struct., vol. 42, 2004, pp. 1445–1464.

Singer, J.; Arboz, J.; and Weller, T.: Buckling Experiments: Experimental Methods in Buckling Thin-Walled Structures: Basic Concepts, Columns, Beams and Plates. Vol. 1, John Wiley & Sons, Inc., New York, NY, 1998.

Schultz, Marc R.; and Nemeth, Michael P.: Buckling Imperfection Sensitivity of Axially Compressed Orthotropic Cylinders. AIAA 2010–2531, 2010.

Vinson, Jack R.: The Behavior of Sandwich Structures of Isotropic and Composite Materials. CRC Press, Boca Raton, FL, 1999.

Zalewski, Bart F.; Dial, William B.; and Bednarcyk, Brett A.: Methods for Assessing Honeycomb Sandwich Panel Wrinkling Failures. NASA/TM—2012-217697, 2012. http://ntrs.nasa.gov